

---

# E-PINNs: EPISTEMIC PHYSICS-INFORMED NEURAL NETWORKS

---

✉ **Ashish S. Nair**

University of Notre Dame  
South Bend, IN 46637  
anair@nd.edu

✉ **Bruno Jacob**

Pacific Northwest National Laboratory  
Richland, WA 99354  
bruno.jacob@pnnl.gov

✉ **Amanda A. Howard**

Pacific Northwest National Laboratory  
Richland, WA 99354  
amanda.howard@pnnl.gov

✉ **Jan Drgona**

Pacific Northwest National Laboratory  
Richland, WA 99354  
jan.drgona@pnnl.gov

✉ **Panos Stinis**

Pacific Northwest National Laboratory  
Richland, WA 99354  
panagiotis.stinis@pnnl.gov

March 26, 2025

## ABSTRACT

Physics-informed neural networks (PINNs) have demonstrated promise as a framework for solving forward and inverse problems involving partial differential equations. Despite recent progress in the field, it remains challenging to quantify uncertainty in these networks. While approaches such as Bayesian PINNs (B-PINNs) provide a principled approach to capturing uncertainty through Bayesian inference, they can be computationally expensive for large-scale applications. In this work, we propose Epistemic Physics-Informed Neural Networks (E-PINNs), a framework that leverages a small network, the *epinet*, to efficiently quantify uncertainty in PINNs. The proposed approach works as an add-on to existing, pre-trained PINNs with a small computational overhead. We demonstrate the applicability of the proposed framework in various test cases and compare the results with B-PINNs using Hamiltonian Monte Carlo (HMC) posterior estimation and dropout-equipped PINNs (Dropout-PINNs). Our experiments show that E-PINNs provide similar coverage to B-PINNs, with often comparable sharpness, while being computationally more efficient. This observation, combined with E-PINNs' more consistent uncertainty estimates and better calibration compared to Dropout-PINNs for the examples presented, indicates that E-PINNs offer a promising approach in terms of accuracy-efficiency trade-off.

**Keywords** Physics-informed neural networks · Uncertainty quantification · Epistemic neural networks

## 1 Introduction

Uncertainty quantification is a critical component in the deployment of machine learning models for scientific and engineering applications. Physics-Informed Neural Networks (PINNs) have shown promise in solving partial differential equations (PDEs) by incorporating physical laws directly into the learning process [1]. PINNs have been successfully applied to a diverse range of scientific and engineering problems, including fluid dynamics and turbulence [2, 3, 4, 5], heat transfer [6, 7, 8, 9], biomedical applications [10, 11, 12], electromagnetic systems [13, 14], among many other applications. When employing neural networks to physics-informed tasks, it is crucial to ensure that the models are not only accurate but also provide insights into the confidence of their predictions. However, traditional PINNs do not inherently quantify uncertainty, which is essential in decision-making processes for complex systems [15].

Uncertainty is typically classified into two types: aleatoric or epistemic uncertainty. Aleatoric refers to the uncertainty inherent in the data, often due to noise or stochasticity in the physical process being modeled. This type of uncertainty cannot be reduced by collecting more data. In contrast, epistemic uncertainty arises due to limited data or lack of knowledge about the model itself and can be reduced with more data or a better model [16, 17]. Understanding and

distinguishing between these types of uncertainty is crucial for robust modeling, particularly in scientific applications where decision-making based on model predictions can have significant consequences.

The field of uncertainty quantification in deep learning has seen substantial growth in recent years. Bayesian Neural Networks (BNNs) provide a principled approach to uncertainty quantification by placing prior distributions over model parameters and inferring posterior distributions through Bayesian inference [18, 19, 20]. These methods naturally account for both aleatoric and epistemic uncertainty through their probabilistic formulation. However, they often face scalability challenges when applied to complex models or high-dimensional data [21].

Ensemble methods represent another prominent approach to uncertainty quantification, where multiple models are trained, and their predictions aggregated to estimate uncertainty [22]. While effective in practice, these methods can be computationally expensive as they require training multiple independent models. Deep ensembles, in particular, have demonstrated strong performance in capturing predictive uncertainty by training neural networks with different random initializations [23]. However, research has shown that naively pooling ensemble predictions can sometimes lead to under-confidence in the model’s predictions [24].

As an alternative to the computationally intensive Bayesian and ensemble methods, dropout methods offer a computationally lighter approach for uncertainty quantification. Dropout approximates Bayesian inference through the random deactivation of neurons during both training and inference, effectively sampling from a posterior distribution over the network parameters without explicitly performing Bayesian sampling [25, 26, 27, 28]. This method has been widely adopted due to its simplicity and effectiveness, though its theoretical underpinnings and optimal configuration remain areas of active research [29].

In the context of scientific machine learning, uncertainty quantification takes on added importance due to the critical nature of many scientific and engineering applications. Recent approaches have focused on integrating physical principles into the uncertainty quantification process. Physics-informed Bayesian Neural Networks have been proposed to combine the expressiveness of neural networks with the physical constraints imposed by governing equations [30, 31]. These methods aim to respect physical laws while providing probabilistic predictions, though they often face challenges related to the balance between data-driven learning and physical consistency. For PINNs [1] specifically, several uncertainty quantification methods have been developed. Bayesian PINNs (B-PINNs) incorporate prior knowledge about physical systems while quantifying both aleatoric and epistemic uncertainties through a principled Bayesian treatment [15]. However, they often struggle with scalability due to the high computational cost of sampling from the posterior distribution over the model parameters, and may suffer from high variance in the predictive distribution, particularly in high-dimensional spaces or when data is sparse [32].

Dropout has also been applied to PINNs (hereinafter referred to as Dropout-PINNs), providing a more computationally efficient alternative to B-PINNs [32, 15]. However, the choice of dropout rate significantly impacts the quality of uncertainty quantification, which may limit the applicability of Dropout-PINNs in scenarios involving complex physical phenomena or sparse training data [15].

In the broader context of operator learning, uncertainty quantification for neural operators, including deep operator networks (DeepONets) [33], has gained attention. These models aim to learn mappings between function spaces. Approaches such as randomized prior methods [34], ensemble methods [35], and Bayesian formulations [36, 37] have been proposed to quantify uncertainty in operator learning settings. These methods are particularly important when the input-output mappings are complex or when dealing with noisy or incomplete data, which is common in scientific applications.

A recent promising direction involves combining conformal prediction methods with PINNs [38] and DeepONets [39]. Conformal methods construct distribution-free uncertainty intervals that offer rigorous finite-sample coverage guarantees without relying on Bayesian assumptions or computationally intensive sampling. For example, conformalized DeepONets utilize split conformal prediction to generate robust confidence intervals directly from neural operator predictions [39]. However, both approaches inherit fundamental conformal prediction limitations: they require representative calibration datasets that match future test distributions, and they sacrifice some training data for the calibration process [40].

## 1.1 Contributions and Novelty of the Present Work

In the present work, we propose epistemic physics-informed neural networks (E-PINNs), a novel extension of the traditional PINN framework designed to quantify total uncertainty. Our approach builds upon the concept of epistemic neural networks [41], which provides a flexible framework for modeling uncertainty by introducing a source of randomness into the model parameters or inputs. We provide comprehensive empirical evaluations comparing E-PINNs with B-PINNs and Dropout-PINNs on forward initial-boundary value problems. Additionally, we conduct ablation

studies investigating the sensitivity of E-PINNs to various hyperparameters including network size, number of samples and magnitude of noise. These analyses provide insights into the robustness and practical applicability of our approach.

The key innovation of our E-PINN framework lies in its architecture: we connect an epinet, a small neural network perturbed by random variables at its input, with a base PINN. This design offers several advantages over existing methods. First, unlike Bayesian approaches that require sampling from posterior distributions over all parameters, our method introduces randomness in a controlled and efficient manner through the epinet. Unlike B-PINNs, which face scalability challenges when sampling from high-dimensional posterior distributions, E-PINNs maintain computational efficiency even for complex models. Second, unlike dropout-based methods that randomly deactivate neurons throughout the network and implicitly entangle data and model uncertainty, our approach allows for an explicit separation of the two. In addition, while dropout-based methods are highly sensitive to the dropout rate, our approach provides more stable uncertainty estimates across a range of hyperparameter settings, as demonstrated in our ablation studies.

A significant contribution of our work is the flexibility of the E-PINN framework. The epinet can be trained in conjunction with the PINN, allowing for end-to-end uncertainty-aware learning. Alternatively, it can be trained independently after a base PINN has been trained, enabling uncertainty quantification as a post-processing step. This latter capability is particularly valuable for practitioners who already have trained PINNs and wish to add uncertainty quantification without retraining the entire model, introducing only a small computational overhead.

This work is organized as follows: In Sec. 2, we present three frameworks for uncertainty quantification in PINNs: B-PINNs, Dropout-PINNs and E-PINNs. In Sec. 3, we compare the performance of these methods in forward initial-boundary value problems, along with ablation studies for the sensitivity of hyperparameters of E-PINNs (network size, learning rate, and epistemic index distribution) in the uncertainty quantification. Finally, a summary of the findings is presented in Sec. 4.

## 2 Methods

In this section, we detail the methodologies employed for uncertainty quantification in PINNs. We explore three primary approaches: B-PINNs, Dropout-PINNs and E-PINNs. Each method offers distinct mechanisms for capturing and quantifying uncertainty in model predictions.

In all methods, we consider a general PDE of the form

$$\mathcal{N}_x(u; \lambda) = f(x), \quad x \in D, \quad (1)$$

$$\mathcal{B}_x(u; \lambda) = b(x), \quad x \in \partial D, \quad (2)$$

where  $\mathcal{N}_x$  represents a general differential operator,  $\mathcal{B}_x$  denotes a general boundary operator,  $u(x)$  is the solution to the PDE,  $\lambda$  is a vector of parameters in the PDE,  $f(x)$  is a source term, and  $b(x)$  specifies the boundary conditions. The domain  $D \subset \mathbb{R}^d$  is a  $d$ -dimensional spatial domain, and  $\partial D$  denotes its boundary.

### 2.1 Bayesian physics-informed neural networks

B-PINNs [15] extend the traditional PINN framework by incorporating BNNs [18, 20] to quantify uncertainty in the model predictions. This approach treats the neural network parameters as random variables with specified prior distributions, allowing for the estimation of posterior distributions given observed data and physical constraints [15, 42, 43, 44].

In this framework, the solution  $u(x)$  is approximated by a surrogate model  $\tilde{u}_\theta(x)$ , where  $\theta$  denotes the neural network parameters. The prior distribution over  $\theta$ , denoted as  $P(\theta)$ , encapsulates our initial beliefs about the network parameters before observing any data.

The PDE constraints are incorporated into the prior by ensuring that  $\tilde{u}_\theta(x)$  satisfies the PDE (1) and boundary conditions (2) to the extent dictated by the neural network architecture and activation functions. Specifically, the forcing term and boundary conditions are modeled as:

$$\tilde{f}_\theta(x) = \mathcal{N}_x(\tilde{u}_\theta(x); \lambda), \quad (3)$$

$$\tilde{b}_\theta(x) = \mathcal{B}_x(\tilde{u}_\theta(x); \lambda). \quad (4)$$

We assume a dataset  $\mathcal{D}$  containing independently distributed noisy measurements of  $u$ ,  $f$ , and  $b$ , denoted as  $\mathcal{D} = \mathcal{D}_u \cup \mathcal{D}_f \cup \mathcal{D}_b$ , where

$$\mathcal{D}_u = \{(x_i^u, \bar{u}_i)\}_{i=1}^{N_u}, \quad \bar{u}_i = u(x_i^u) + \epsilon_i^u, \quad (5)$$

$$\mathcal{D}_f = \{(x_i^f, \bar{f}_i)\}_{i=1}^{N_f}, \quad \bar{f}_i = f(x_i^f) + \epsilon_i^f, \quad (6)$$

$$\mathcal{D}_b = \{(x_i^b, \bar{b}_i)\}_{i=1}^{N_b}, \quad \bar{b}_i = b(x_i^b) + \epsilon_i^b, \quad (7)$$

and  $N_u, N_f, N_b$  denote the number of measurements, and  $\epsilon_i^u, \epsilon_i^f, \epsilon_i^b$  are independent Gaussian noises with zero mean and known variances,  $\sigma_i^u, \sigma_i^f, \sigma_i^b$ , i.e.,  $\epsilon_i^u \sim \mathcal{N}(0, \sigma_i^u)$ ,  $\epsilon_i^f \sim \mathcal{N}(0, \sigma_i^f)$ , and  $\epsilon_i^b \sim \mathcal{N}(0, \sigma_i^b)$ .

In this scenario, the likelihood function is defined as:

$$P(\mathcal{D}|\theta) = P(\mathcal{D}_u|\theta) P(\mathcal{D}_f|\theta) P(\mathcal{D}_b|\theta), \quad (8)$$

where  $P(\theta)$  is the prior for hyperparameters and unknown PDE terms,  $P(\mathcal{D}|\theta)$  is the likelihood of observations and  $P(\theta|\mathcal{D})$  is the posterior. Applying Bayes' theorem, the posterior distribution of the parameters  $\theta$  given the data  $\mathcal{D}$  is given by

$$P(\theta|\mathcal{D}) = \frac{P(\mathcal{D}|\theta) P(\theta)}{P(\mathcal{D})} \simeq P(\mathcal{D}|\theta) P(\theta), \quad (9)$$

where  $P(\mathcal{D})$  denotes the marginal likelihood, often intractable to compute directly, and  $\simeq$  denotes equality up to a constant [15]. As a consequence, sampling methods, such as Hamiltonian Monte Carlo (HMC) [20, 45] or variational inference (VI) [21, 19] are then employed to approximate the posterior distribution. Thus, a posterior  $u(x)$  can be sampled from  $P(\theta|\mathcal{D})$ , resulting in  $\{\tilde{u}_{\theta^{(i)}}(x)\}_{i=1}^M$  samples. Mean predictions and total uncertainty are then quantified with the mean and standard deviation of  $\{\tilde{u}_{\theta^{(i)}}(x)\}_{i=1}^M$ , respectively.

It is important to note that this Bayesian formulation naturally captures both types of uncertainty. The aleatoric uncertainty is explicitly modeled through the noise terms in the measurement model ( $\epsilon_i^u, \epsilon_i^f, \epsilon_i^b$ ), while the epistemic uncertainty is captured through the posterior distribution over the network parameters  $P(\theta|\mathcal{D})$ . When sampling from the posterior to obtain  $\{\tilde{u}_{\theta^{(i)}}(x)\}_{i=1}^M$ , the variance of these samples represents the total uncertainty, combining both the uncertainty inherent in the data (aleatoric) and the uncertainty in our model parameters (epistemic).

Given the low performance of B-PINN-VI reported by [15], in this work we will use only B-PINN-HMC when referring to B-PINNs in the tests and comparisons presented in Sec. 4.

## 2.2 Dropout-based physics-informed neural networks

Dropout-PINNs incorporate dropout layers within the neural network architecture as a means to quantify total uncertainty [32]. Dropout, originally introduced as a regularization technique to prevent overfitting [46], randomly deactivates a subset of neurons during training, effectively sampling from an ensemble of sub-networks.

In the context of PINNs, dropout is applied during both training and inference phases. During training, it regularizes the network by preventing co-adaptation of neurons, while during inference, it enables uncertainty quantification through Monte Carlo sampling. By performing multiple forward passes with different dropout masks, one can obtain a distribution of predictions that reflects the uncertainty in the model's output. The predictive mean and variance are then computed as:

$$\mathbb{E}[u_\theta(x)] = \frac{1}{M} \sum_{m=1}^M u_{\theta^{(m)}}(x), \quad (10)$$

$$\text{Var}[u_\theta(x)] = \frac{1}{M} \sum_{m=1}^M (u_{\theta^{(m)}}(x) - \mathbb{E}[u_\theta(x)])^2, \quad (11)$$

where  $u_{\theta^{(m)}}$  denotes the output of the model's  $m$ -th forward pass,  $\theta^{(m)}$  represents the network parameters sampled with dropout for the  $m$ -th forward pass, and  $M$  is the total number of Monte Carlo samples.

While dropout provides a computationally efficient method for uncertainty quantification, it has inherent limitations. As reported in [15] the choice of dropout rate significantly influences the quality of the uncertainty estimates, with higher rates potentially leading to underconfident predictions and lower rates risking overfitting [26]. Moreover, dropout-based methods do not adequately represent the full uncertainty spectrum, especially in regions with sparse or no training data [15, 47].

Nevertheless, when compared to Bayesian approaches like B-PINNs, dropout-based methods offer a simpler implementation with lower computational overhead. The method requires minimal modifications to the existing PINN architecture and can be easily integrated into existing frameworks. Furthermore, the computational cost of uncertainty estimation scales linearly with the number of Monte Carlo samples  $M$ , making it particularly attractive for large-scale applications where full Bayesian inference might be computationally prohibitive. In Sec. 4, we use dropout to compare the quality of uncertainty and computational time in various examples.

### 2.3 Epistemic physics-informed neural networks

Epistemic neural networks are a generalization of ensemble-based uncertainty estimation methods proposed by [41]. This framework defines a parameterized function  $u$ , approximated by a neural network with learnable parameters  $\theta$  as  $u_\theta$ , and a reference distribution  $P_z$ , typically chosen as a uniform distribution. An *epistemic index*, denoted by  $z$ , is sampled from  $P_z$  and used to express the epistemic uncertainty of  $u$ . Thus, for an input  $x$  and epistemic index  $z$ , we obtain a realization of the output,  $u_\theta(x, z)$ .

In the present work, we introduce epistemic PINNs (E-PINNs): a modification of the original PINN architecture that supplements the base PINN with an *epinet*, a companion neural network designed to quantify uncertainty in the base network. A diagram of the framework is shown in Fig. 1, and a pseudocode of the algorithm is shown in Algorithm 1.

Formally, given an input feature  $x$  and an epistemic index  $z \sim P_z$ , the E-PINN prediction is given by:

$$\underbrace{u_\theta(x, z)}_{\text{E-PINN output}} = \underbrace{u_\xi(x)}_{\text{base PINN output}} + \underbrace{e_\eta(\tilde{x}, z)}_{\text{epinet output}}, \quad (12)$$

where  $u_\xi(x)$  is the output of the base PINN with trainable parameters  $\xi$ , and  $e_\eta(\tilde{x}, z)$  is the output of the epinet with trainable parameters  $\eta$ . The concatenation of all trainable parameters is denoted by  $\theta = (\xi, \eta)$ . The epinet can be trained in conjunction with the PINN (coupled approach) or separately (decoupled approach, i.e., when the PINN has been pre-trained and has fixed weights). An augmented feature vector, defined as  $\tilde{x} = \text{sg}[\phi_\xi(x)]$ , is generated by combining information from the PINN and its input  $x$  through a function  $\phi$ . The stop gradient operation  $\text{sg}$  blocks the backpropagation from the epinet to the PINN, effectively preventing the information from the posterior from leaking to the prior, when we choose to train the PINN and the epinet simultaneously. We investigate differences in these approaches in Sec. 3.6.1.

The epinet consists of two components: a learnable network, with output  $e_\eta^L(\tilde{x}, z)$ , and a prior network, a network with frozen weights (thus no dependence on  $\eta$ ), with output  $e^P(\tilde{x}, z)$ . Specifically, given inputs  $\tilde{x}$  and epistemic index  $z$ , the output of the epinet is:

$$e_\eta(\tilde{x}, z) = e_\eta^L(\tilde{x}, z) + \alpha e^P(\tilde{x}, z), \quad (13)$$

where  $\alpha$  is a hyperparameter used to scale the effect of the prior epinet. In this work, we set  $\alpha = 1$  for simplicity. We design  $e^P$  as a multilayer perceptron (MLP) with initial weights and biases computed using He initialization [48]. This choice allows for adjustable expressivity of the joint predictions, depending on the depth (number of hidden layers) and width (number of neurons per layer) of  $e_\eta^L$ . For the prior network  $e^P$ , we construct a network with the same architecture as the learnable network but with different initial parameters, as in [41].

Importantly, the epinet output  $e_\eta(\tilde{x}, z)$  is modeled as a random variable even for fixed epistemic index  $z$ . This introduces variability within each  $z$ , allowing us to capture both epistemic and aleatoric uncertainties. Specifically, the internal sources of randomness in  $e_\eta(\tilde{x}, z)$  arise from noisy inputs or noisy source terms in the PDEs (e.g.,  $f$  in (1)), often referred to as noisy sensors [15]. Therefore, for each  $z$ , the epinet output  $e_\eta(\tilde{x}, z)$  has its own mean and variance:

$$m_z(x) = \mathbb{E}[e_\eta(\tilde{x}, z) | z], \quad (14)$$

$$v_z(x) = \text{Var}[e_\eta(\tilde{x}, z) | z], \quad (15)$$

where expectations are taken over the internal sources of randomness introduced by the noisy sensors within the epinet for a given  $z$ . Note that the output  $u_\theta(x, z)$  is a random variable even when  $z$  is fixed, with the mean and variance for each  $z$  given by:

$$u_z(x) = u_\xi(x) + m_z(x), \quad (16)$$

$$v_z(x) = \text{Var}[u_\theta(x, z) | z]. \quad (17)$$

The overall mean prediction and total variance are then calculated using the law of total expectation and the law of total variance:

$$\mu_*(x) = u_\xi(x) + \mathbb{E}_z [m_z(x)], \quad (18)$$

$$\text{Var}_*(x) = \text{Var}_z [u_z(x)] + \mathbb{E}_z [v_z(x)], \quad (19)$$

where  $\text{Var}_z [u_z(x)]$  can be interpreted as epistemic uncertainty due to variability in the mean predictions across different  $z$ . The term  $\mathbb{E}_z [v_z(x)]$  captures the aleatoric uncertainty due to inherent randomness within each  $z$  arising from noisy sensors. This highlights the epinet's capability to distinguish between epistemic and aleatoric uncertainty, providing a comprehensive estimate of the total uncertainty.

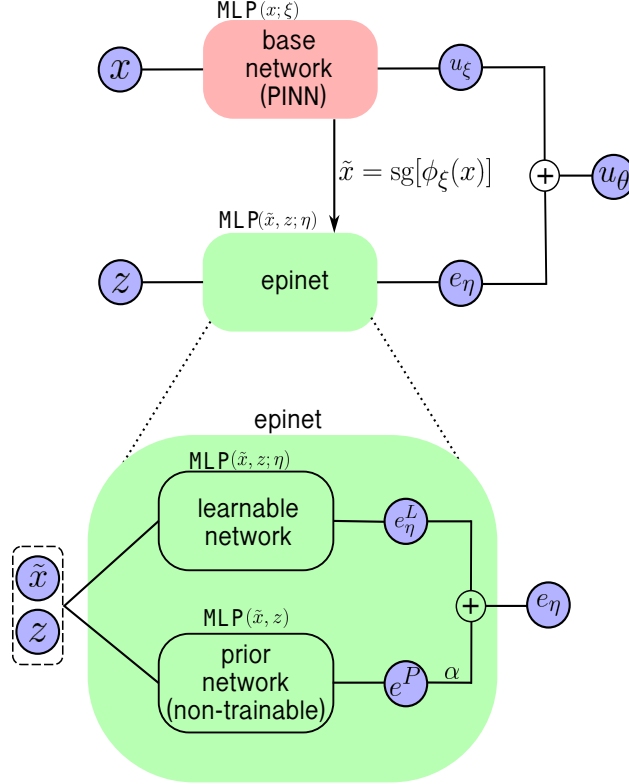


Figure 1: Schematic diagram of the E-PINN architecture. The base PINN (red) produces a deterministic prediction  $u_\xi$ . The epinet (green) receives as input the augmented feature vector  $\tilde{x}$ , computed as the stop-gradient of the base PINN's last hidden-layer activations, and a random epistemic index  $z \sim P_z$ . Internally, the epinet comprises two neural networks: a trainable learnable network producing output  $e_\eta^L$ , and a non-trainable prior network with fixed parameters producing output  $e_\eta^P$ . The final epinet output  $e_\eta$  is a weighted sum of these two components, controlled by the hyperparameter  $\alpha$ . The sum of the epinet output and the base PINN output yields the final stochastic E-PINN prediction  $u_\theta$ .

## 2.4 Loss function and training

For all three uncertainty quantification approaches discussed in this paper (B-PINN, Dropout-PINN, and E-PINN), the underlying training process involves minimizing a composite loss function that incorporates both data observations and physical constraints:

$$\mathcal{L}_{\text{total}} = \lambda_{\text{data}} \mathcal{L}_{\text{data}} + \lambda_{\text{pde}} \mathcal{L}_{\text{pde}} + \lambda_{\text{boundary}} \mathcal{L}_{\text{boundary}}, \quad (20)$$

where  $\lambda_{\text{data}}$ ,  $\lambda_{\text{pde}}$ , and  $\lambda_{\text{boundary}}$  are weighting coefficients that balance the different components of the loss, and:

**Algorithm 1** Epistemic Physics-Informed Neural Networks (E-PINNs)

**Require:**

- 1: PDE operators  $\mathcal{N}_x, \mathcal{B}_x$ , and parameters  $\lambda$
- 2: Training data  $\{(x_i^u, \bar{u}_i)\}_{i=1}^{N_u}, \{(x_i^f, \bar{f}_i)\}_{i=1}^{N_f}, \{(x_i^b, \bar{b}_i)\}_{i=1}^{N_b}$
- 3: Noise standard deviations  $\sigma_u, \sigma_f, \sigma_b$
- 4: Reference distribution  $P_z$  for epistemic index sampling
- 5: Training mode  $\in \{\text{coupled}, \text{decoupled}\}$
- 6: Base PINN parameters  $\xi$  (required only if decoupled)
- 7: **procedure** TRAINEPINN
  - 8: **if** training mode = decoupled **then**
    - 9: Use pre-trained base PINN with fixed parameters  $\xi$
    - 10: Initialize epinet learnable parameters  $\eta^L$
  - 11: **else**
    - 12: Initialize base PINN parameters  $\xi$
    - 13: Initialize epinet learnable parameters  $\eta^L$
  - 14: **end if**
  - 15: Initialize epinet prior network with fixed weights
  - 16: **repeat**
    - 17: Sample collocation points, boundary points, data points
    - 18: Sample epistemic index  $z \sim P_z$
    - 19: /\* Add noise to measurements \*/
    - 20:  $\bar{f}_i \leftarrow f(x_i^f) + \epsilon_i^f$  where  $\epsilon_i^f \sim \mathcal{N}(0, \sigma_f^2)$
    - 21:  $\bar{u}_i \leftarrow u(x_i^u) + \epsilon_i^u$  where  $\epsilon_i^u \sim \mathcal{N}(0, \sigma_u^2)$
    - 22:  $\bar{b}_i \leftarrow b(x_i^b) + \epsilon_i^b$  where  $\epsilon_i^b \sim \mathcal{N}(0, \sigma_b^2)$
    - 23: /\* Forward pass through networks \*/
    - 24:  $u_\xi(x) \leftarrow \text{BasePINN}(x; \xi)$
    - 25:  $\tilde{x} \leftarrow \text{sg}[\phi_\xi(x)]$  ▷ Stop gradient
    - 26:  $e_\eta^L(\tilde{x}, z) \leftarrow \text{LearnableNetwork}(\tilde{x}, z; \eta^L)$
    - 27:  $e^P(\tilde{x}, z) \leftarrow \text{PriorNetwork}(\tilde{x}, z)$
    - 28:  $e_\eta(\tilde{x}, z) \leftarrow e_\eta^L(\tilde{x}, z) + e^P(\tilde{x}, z)$
    - 29:  $u_\theta(x, z) \leftarrow u_\xi(x) + e_\eta(\tilde{x}, z)$
    - 30: /\* Compute losses \*/
    - 31:  $\mathcal{L}_{\text{pde}} \leftarrow \frac{1}{N_f} \sum_{i=1}^{N_f} |\mathcal{N}_x(u_\theta(x_i^f, z); \lambda) - \bar{f}_i|^2$
    - 32:  $\mathcal{L}_{\text{boundary}} \leftarrow \frac{1}{N_b} \sum_{i=1}^{N_b} |\mathcal{B}_x(u_\theta(x_i^b, z); \lambda) - \bar{b}_i|^2$
    - 33:  $\mathcal{L}_{\text{data}} \leftarrow \frac{1}{N_u} \sum_{i=1}^{N_u} |u_\theta(x_i^u, z) - \bar{u}_i|^2$  ▷ (If available)
    - 34:  $\mathcal{L}_{\text{total}} \leftarrow \mathcal{L}_{\text{data}} + \mathcal{L}_{\text{pde}} + \mathcal{L}_{\text{boundary}}$
    - 35: **if** training mode = decoupled **then**
      - 36: Update epinet parameters  $\eta^L$  using optimizer to minimize  $\mathcal{L}_{\text{total}}$
    - 37: **else**
      - 38: Update both base PINN parameters  $\xi$  and epinet parameters  $\eta^L$  to minimize  $\mathcal{L}_{\text{total}}$
    - 39: **end if**
    - 40: **until** desired convergence
  - 41: **end procedure**
  - 42: **procedure** ESTIMATEUNCERTAINTY( $x, M$ )
    - 43:  $\{u_i\}_{i=1}^M \leftarrow \emptyset$  ▷ Initialize array for predictions
    - 44: **for**  $i = 1$  to  $M$  **do**
      - 45: Sample  $z_i \sim P_z$
      - 46:  $u_i \leftarrow u_\xi(x) + e_\eta(\tilde{x}, z_i)$
    - 47: **end for**
    - 48:  $\mu_*(x) \leftarrow \frac{1}{M} \sum_{i=1}^M u_i$  ▷ Mean prediction
    - 49:  $\text{Var}_*(x) \leftarrow \frac{1}{M} \sum_{i=1}^M (u_i - \mu_*(x))^2$  ▷ Total variance
    - 50: **return**  $\mu_*(x), \text{Var}_*(x)$
    - 51: **end procedure**

$$\mathcal{L}_{\text{data}} = \frac{1}{N_u} \sum_{i=1}^{N_u} |u_\theta(x_i^u) - \bar{u}_i|^2, \quad (21)$$

$$\mathcal{L}_{\text{pde}} = \frac{1}{N_f} \sum_{i=1}^{N_f} |\mathcal{N}_x(u_\theta(x_i^f); \lambda) - \bar{f}_i|^2, \quad (22)$$

$$\mathcal{L}_{\text{boundary}} = \frac{1}{N_b} \sum_{i=1}^{N_b} |\mathcal{B}_x(u_\theta(x_i^b); \lambda) - \bar{b}_i|^2. \quad (23)$$

The weighting parameters can be adjusted manually or in a self-adaptive manner [49, 50, 51]. For simplicity, we assume  $\lambda_{\text{data}} = \lambda_{\text{pde}} = \lambda_{\text{boundary}} = 1$ .

The term  $\mathcal{L}_{\text{data}}$  represents the mean squared error between the network predictions and the available data measurements,  $\mathcal{L}_{\text{pde}}$  enforces the PDE residual at the collocation points within the domain, and  $\mathcal{L}_{\text{boundary}}$  ensures that the solution satisfies the prescribed boundary conditions.

The network parameters  $\theta$  are optimized by solving the minimization problem:

$$\theta^* = \arg \min_{\theta} \mathcal{L}_{\text{total}}(\theta). \quad (24)$$

This minimization problem is solved approximately using the Adam optimization algorithm. All networks in this work are trained with the Adam optimizer, with learning rate  $l = 10^{-3}$ , exponential decay rates for the first and second moment estimates  $\beta_1 = 0.9$  and  $\beta_2 = 0.999$ , respectively.

### 3 Results

In this section, we compare the three uncertainty quantification methods introduced in Section 2. The goal is to illustrate the applicability of the proposed E-PINN framework in estimating epistemic uncertainty in various scenarios, to evaluate computational costs, and to provide a qualitative assessment of the resulting uncertainty bands.

In our evaluation of uncertainty quantification methods, we focus on two metrics: sharpness and coverage. Sharpness refers to the width of predictive intervals, while coverage indicates how often these intervals contain the true values [52, 53]. As noted by [53], prediction intervals should ideally be narrow while still capturing the expected proportion of observations.

We quantify *sharpness* as the average width of the  $\pm 2\sigma$  predictive intervals [52]:

$$\mu_{2\sigma}^w = \frac{4}{N} \sum_{i=1}^N \sqrt{\text{Var}_*(x_i)}, \quad (25)$$

where  $N$  denotes the number of points at which the total variance  $\text{Var}_*(x_i)$  is evaluated. Smaller values of  $\mu_{2\sigma}^w$  indicate sharper uncertainty estimates.

In addition to sharpness, we evaluate the quality of uncertainty estimates using *empirical coverage*, which measures the percentage of true values that fall within the predicted uncertainty bounds [54]. Specifically, for a given confidence level  $\gamma$  (typically 95% corresponding to  $\pm 2\sigma$  bounds), the empirical coverage is calculated as:

$$C_\gamma = \frac{1}{N} \sum_{i=1}^N \mathbf{1}\{|u(x_i) - \mu_*(x_i)| \leq q_{\gamma/2} \sqrt{\text{Var}_*(x_i)}\}, \quad (26)$$

where  $\mathbf{1}\{\cdot\}$  is the indicator function,  $u(x_i)$  is the true (exact) value,  $\mu_*(x_i)$  and  $\text{Var}_*(x_i)$  are the predicted mean and variance at point  $x_i$ , and  $q_{\gamma/2}$  is the appropriate quantile of the standard normal distribution (approximately 1.96 for  $\gamma = 0.95$ ). An ideal uncertainty quantification method should achieve an empirical coverage close to the specified confidence level: a value too low indicates overconfidence, while too high suggests overly conservative models. [54].

To ensure a fair comparison of these metrics across methods, we implement the three uncertainty quantification approaches with consistent settings. For the B-PINN results, we follow [15] and set the HMC mass matrix to be the identity matrix, and take a leapfrog step  $L = 50\delta t$ , initial time step  $\delta t = 0.1$ , with 2,000 burn-in steps and  $M = 15,000$  samples.



Table 1: Comparison of sharpness  $\mu_{2\sigma}^w$  for the function regression test case

Sensor Noise	BNN	ENN	Dropout-NN (5%)	Dropout-NN (20%)
$\epsilon \sim \mathcal{N}(0, 0.3^2)$	0.83	<b>0.71</b>	1.61	3.50
$\epsilon \sim \mathcal{N}(0, 0.5^2)$	<b>1.16</b>	1.19	1.56	3.39

For the Dropout-PINNs, the same dropout rate is used during training and inference. The uncertainty bands, computed via mean and standard deviation, are produced by making forward passes in the network  $M = 10,000$  times, thus producing  $M$  trajectories. Dropout-PINNs are trained with the same number of sensors as the E-PINNs and B-PINNs to enable a fair comparison of the different methods.

Throughout the paper, except in Sec. 3.6.1, results of E-PINNs assume that epinets and PINNs are trained in a decoupled fashion: a pre-trained PINN (trained without noise) is used as base network for an epinet. The epinet is trained with noise added to sensor data, and both PINN and epinet share the same loss function. Unless otherwise specified, the PINN and epinets consist of MLPs with two fully connected layers with 32 neurons each.

### 3.1 Function regression

In this first example, we consider a simple regression to compare the three methods highlighted in Sec. 2. Due to the lack of physics constraints, the PINN component of all methods is reduced to a simple MLP (for Dropout-PINN and E-PINN), or a BNN (for B-PINNs). For clarity, we refer to these simplified cases as Dropout-NN, ENN and BNN.

The test function is given by

$$u(x) = \sin^3(x), \quad x \in [-1, 1], \quad (27)$$

where 100 uniformly distributed collocation points in  $x \in [-1, 1]$  are used to train the neural networks. For all cases, 32 point sensors are used for  $u$ , uniformly distributed in  $x \in [-0.8, -0.2] \cup [0.2, 0.8]$ . We consider two cases of observation noise  $\epsilon_u \in \mathcal{N}(0, 0.3^2)$  and  $\epsilon_u \in \mathcal{N}(0, 0.5^2)$ , where  $\mathcal{N}(0, 0.3^2)$  and  $\mathcal{N}(0, 0.5^2)$  represent a normal distribution with noise 30% and 50%, respectively.

Figure 2 compares the mean prediction and the predicted uncertainty bands for the uncertainty quantification methods, given  $\epsilon_u \in \mathcal{N}(0, 0.3^2)$ . The BNN mean prediction is notably inaccurate near domain boundaries, where the absence of sensors leads to expected higher uncertainty. Here, the exact solution lies outside the uncertainty bounds. For Dropout-NN, the mean prediction closely matches the exact solution where  $u$  sensors are densely located, though the prediction accuracy decreases toward the center of the domain. Increasing the dropout rate to 5% results in less accurate mean predictions and larger uncertainty bands, reflecting the dropout-MLP measurement of the total uncertainty of the system. In contrast, the E-MLP predictions show high accuracy in regions with dense sensor coverage, keeping the exact solution within the uncertainty bounds. Compared to BNN and Dropout-NN, the uncertainty bands predicted by ENN are smaller, consistent with measuring total uncertainty, which stems primarily from sensor data noise as the underlying neural network was trained with minimal loss and without added noise.

Figure 3 illustrates the mean predictions and uncertainty bands for  $\epsilon_u \in \mathcal{N}(0, 0.5^2)$ . With an increase in noise in  $u$ , all methods show a notable increase in uncertainty bar size, as expected. BNN, which capture aleatoric uncertainty (data-related uncertainty), show a substantial increase in uncertainty bar size, consistent with the rise in noise levels. For Dropout-NN and ENN, the mean solution accuracy decreases slightly with the added noise in  $u$ . The size of the uncertainty bands predicted by ENN increases with the increase in the data noise, as anticipated, since ENN quantifies total uncertainty which includes the aleatoric uncertainty.

Tables 1 and Table 2 summarize the average width of the uncertainty bands and the empirical coverage for the different methods. It can be observed that both E-PINNs and Dropout-PINNs achieve empirical coverage 1.00 across both noise levels, though this comes at different costs in terms of sharpness: E-PINNs maintain relatively sharp bands ( $\mu_{2\sigma}^w = 0.71$  and 1.19), while Dropout-PINNs produce much wider bands. In contrast, the empirical coverage for B-PINNs (0.84-0.86) falls below the 95% confidence level, indicating overconfidence despite their competitive sharpness.

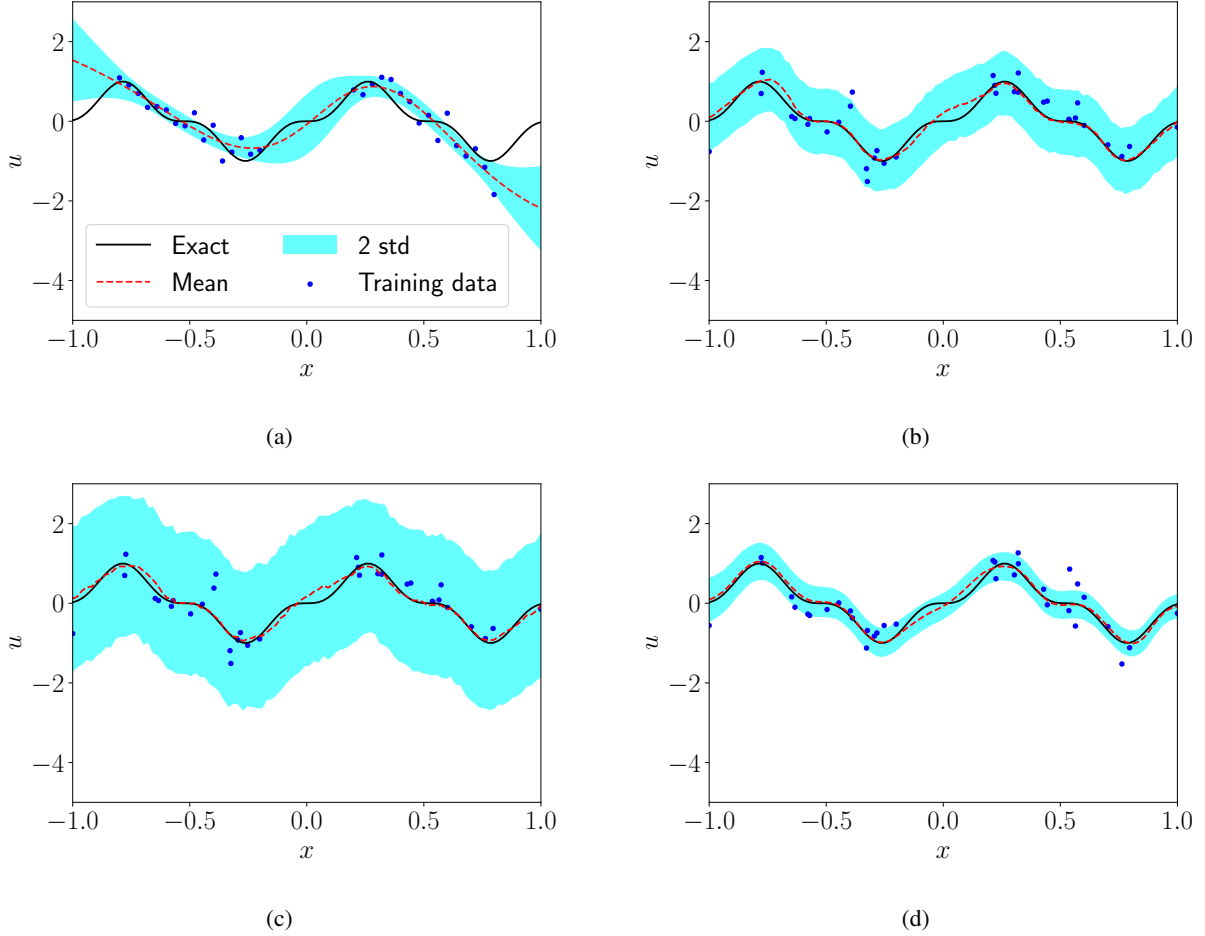


Figure 2: Mean and uncertainty bands predictions for  $u$  in a function regression test case with  $\epsilon_u \sim \mathcal{N}(0, 0.3^2)$  using (a) BNN (b) Dropout-NN with 5% drop rate (c) Dropout-NN with 20% drop rate (d) ENN.

Table 2: Comparison of empirical coverage  $C_\gamma$  for the function regression test case

Sensor Noise	BNN	ENN	Dropout-NN (5%)	Dropout-NN (20%)
$\epsilon \sim \mathcal{N}(0, 0.3^2)$	0.84	<b>1.00</b>	<b>1.00</b>	<b>1.00</b>
$\epsilon \sim \mathcal{N}(0, 0.5^2)$	0.86	<b>1.00</b>	<b>1.00</b>	<b>1.00</b>

### 3.2 1D Poisson equation

In this section we consider the 1D Poisson equation, given by

$$\lambda \frac{\partial^2 u}{\partial x^2} = f, \quad x \in [-0.7, 0.7], \quad (28)$$

with exact solution

$$u(x) = \sin^3(x). \quad (29)$$

The analytical form for  $f$  can be computed by substituting Eq. 29 into Eq. 28. The base PINN is trained using 100 uniformly distributed collocation points in  $x \in [-0.7, 0.7]$ , including sensors at the boundaries. The B-PINN, E-PINN and Dropout-PINN are trained using 16 sensors for  $f$  which are uniformly distributed in  $x \in [-0.7, 0.7]$  along with two sensors for  $u$  at  $x = -0.7$  and  $x = 0.7$  respectively to enforce the boundary conditions. Sensor noise is only added to the  $f$  measurements. For Dropout-PINNs and E-PINNs, the predicted  $f$  is calculated using a second-order central difference scheme, from the predicted  $u$  solution.

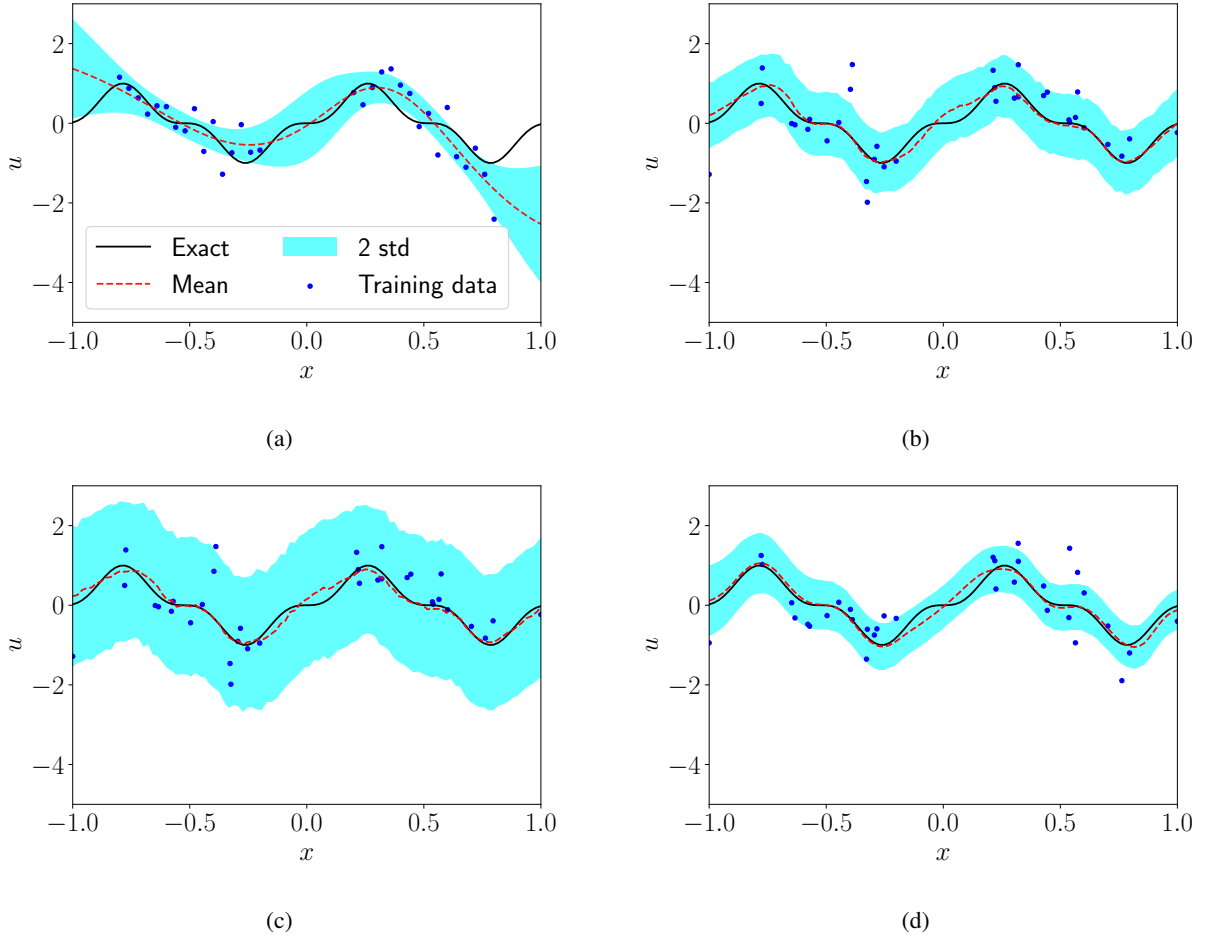


Figure 3: Mean and uncertainty predictions for  $u$  in a function regression test case with  $\epsilon_u \sim \mathcal{N}(0, 0.5^2)$  using (a) BNN (b) Dropout-NN with 2% drop rate (c) Dropout-NN with 5% drop rate (d) ENN.

Figures 4 and 5 show the mean and uncertainty predictions for  $u$  and  $f$  under sensor noise levels  $\epsilon_f \sim \mathcal{N}(0, 0.01^2)$  and  $\epsilon_f \sim \mathcal{N}(0, 0.1^2)$ . In Fig. 4, the exact solution for  $u$  falls within the predicted uncertainty bounds for all three methods. For Dropout-PINNs, the uncertainty bands expand as the dropout rate increases, as expected. Meanwhile, E-PINN yields lower uncertainty in  $f$  predictions compared to B-PINN and Dropout-PINNs, consistent with the noiseless training of the underlying PINN in the E-PINN framework. In contrast, the Dropout-PINN predictions for  $f$  are particularly noisy and inaccurate throughout the domain.

In Fig. 5, the mean predictions for  $u$  and  $f$  by B-PINNs become inaccurate with increasing noise in the sensor measurements  $f$ , and the uncertainty bands expand, as expected for B-PINNs measuring aleatoric uncertainty. The Dropout-PINNs show no significant change in uncertainty bar size with increased sensor noise, though the mean predictions for  $u$  become less accurate. For E-PINNs, while the mean predictions worsen, there is marginal change in the size of the uncertainty bands with increased sensor noise.

Tables 3 and Table 4 summarize the average width of the uncertainty bands and the empirical coverage for the different methods. It can be observed that all methods achieve empirical coverage values close to 1.00 across both noise levels for this test case. Additionally, E-PINNs consistently maintain relatively sharper uncertainty bands compared to the corresponding B-PINN and Dropout-PINN solutions, indicating more precise uncertainty estimates.

### 3.3 1D flow through porous media

This section considers the flow through a horizontal channel filled with a porous medium governed by the equation

Table 3: Comparison of sharpness  $\mu_{2\sigma}^w$  for the 1D Poisson test case

Sensor Noise	B-PINN	E-PINN	Dropout-PINN (2%)	Dropout-PINN (5%)
$\epsilon \sim \mathcal{N}(0, 0.01^2)$	0.81	<b>0.47</b>	0.64	1.47
$\epsilon \sim \mathcal{N}(0, 0.1^2)$	1.52	0.72	<b>0.59</b>	1.36

 Table 4: Comparison of empirical coverage  $C_\gamma$  for the 1D Poisson test case

Sensor Noise	B-PINN	E-PINN	Dropout-PINN (2%)	Dropout-PINN (5%)
$\epsilon \sim \mathcal{N}(0, 0.01^2)$	1.00	<b>0.91</b>	1.00	1.00
$\epsilon \sim \mathcal{N}(0, 0.1^2)$	<b>1.00</b>	<b>1.00</b>	0.88	<b>1.00</b>

$$-\frac{\nu_e}{\phi} \frac{\partial^2 u}{\partial x^2} + \frac{\nu u}{K} = f, \quad x \in [0, 1], \quad (30)$$

with exact solution given by [15],

$$u(x) = \frac{fK}{\nu} \left[ 1 - \frac{\cosh\left(r\left(x - \frac{H}{2}\right)\right)}{\cosh\left(\frac{rH}{2}\right)} \right], \quad (31)$$

and

$$r = \sqrt{\frac{\nu\phi}{\nu_e K}}. \quad (32)$$

For this case, we take the effective viscosity as  $\nu_e = 10^{-3}$ , fluid viscosity  $\nu = 10^{-3}$ , porosity  $\phi = 0.4$ , permeability  $K = 10^{-3}$  and channel height  $H = 1$ . No-slip boundary conditions are imposed on the walls, with  $u(x) = 0$  at  $x = 0, 1$ . Data is collected from sensors for the external force,  $f = 1$ , and noise is added for the different experiments. The base PINN is trained using 100 collocation points uniformly distributed in  $x \in [0, 1]$ , and sensors at the boundaries. The B-PINN, E-PINN and Dropout-PINNs are trained using 16 sensors for the right-hand side term  $f$  which are uniformly distributed in  $x \in [0, 1]$  along with two sensors for  $u$  at  $x = 0$  and  $x = 1$  to enforce the Dirichlet boundary conditions.

Figures 6 and 7 display the mean and uncertainty predictions for  $u$  under sensor noise levels  $\epsilon_f \sim \mathcal{N}(0, 0.01^2)$  and  $\epsilon_f \sim \mathcal{N}(0, 0.1^2)$ , respectively. In Fig. 6, all three methods show accurate mean predictions, even near channel boundaries where steep flow gradients are present, with exact solutions falling within the predicted uncertainty bounds. For Dropout-PINNs, the uncertainty bands increase with a higher dropout rate, consistent with previous cases.

In Fig. 7, with higher noise  $\epsilon_f \sim \mathcal{N}(0, 0.1^2)$ , note that the mean predictions obtained with B-PINN become inaccurate, especially in regions of steep  $u$  gradients. The increased noise has minimal impact on Dropout-PINN's uncertainty predictions, while the E-PINN predictions show deteriorating mean accuracy as sensor noise rises. The uncertainty band width for E-PINN shows a clear increase, consistent with the increase in sensor noise. Table 5 summarizes the average width of the uncertainty bands for the different methods.

Tables 5 and Table 6 summarize the average width of the uncertainty bands and the empirical coverage for the different methods. The results indicate that all methods achieve empirical coverage values close to 1.00 across both noise levels for this test case, except for the B-PINN at the 10% noise level. In this scenario, the B-PINNs produce significantly sharper uncertainty bands; however, this sharpness comes at the cost of overly confident predictions, particularly evident in the 10% noise case.

 Table 5: Comparison of sharpness  $\mu_{2\sigma}^w$  for the 1D flow through porous media test case

Sensor Noise	B-PINN	E-PINN	Dropout-PINN (2%)	Dropout-PINN (5%)
$\epsilon \sim \mathcal{N}(0, 0.01^2)$	<b>0.11</b>	0.47	0.73	1.66
$\epsilon \sim \mathcal{N}(0, 0.1^2)$	<b>0.24</b>	0.76	0.73	1.64

Table 6: Comparison of coverage  $C_\gamma$  for the 1D flow through porous media test case

Sensor Noise	B-PINN	E-PINN	Dropout-PINN (2%)	Dropout-PINN (5%)
$\epsilon \sim \mathcal{N}(0, 0.01^2)$	<b>1.00</b>	<b>1.00</b>	<b>1.00</b>	<b>1.00</b>
$\epsilon \sim \mathcal{N}(0, 0.1^2)$	<b>0.91</b>	1.00	1.00	1.00

Table 7: Comparison of sharpness  $\mu_{2\sigma}^w$  for the 1D nonlinear Poisson equation test case

Sensor Noise	B-PINN	E-PINN	Dropout-PINN (2%)	Dropout-PINN (5%)
$\epsilon \sim \mathcal{N}(0, 0.01^2)$	0.78	<b>0.38</b>	0.93	1.16
$\epsilon \sim \mathcal{N}(0, 0.1^2)$	<b>0.17</b>	0.73	0.56	1.27

### 3.4 1D nonlinear Poisson equation

In this section we consider the 1D nonlinear Poisson equation, given by,

$$\lambda \frac{\partial^2 u}{\partial x^2} + k \tanh(u) = f, \quad x \in [-0.7, 0.7], \quad (33)$$

with exact solution given by,

$$u(x) = \sin^3(x), \quad (34)$$

with constants  $\lambda = 0.01$  and  $k = 0.7$ . The analytical form for  $f$  can be computed by substituting Eq. 34 into Eq. 33. The base PINN is trained using 100 collocation points uniformly distributed in  $x \in [-0.7, 0.7]$ . The B-PINN, E-PINN and Dropout-PINNs are trained using 16 sensors for  $f$  which are uniformly distributed in  $x \in [-0.7, 0.7]$  along with two sensors for  $u$  at  $x = -0.7$  and  $x = 0.7$  respectively to enforce the boundary conditions. Sensor noise is only added to the  $f$  measurements.

Figures 8 and 9 illustrate the predicted mean and uncertainty estimates for  $u$  under sensor noise levels of  $\epsilon_f \sim \mathcal{N}(0, 0.01^2)$  and  $\epsilon_f \sim \mathcal{N}(0, 0.1^2)$ , respectively. In Fig. 8, the B-PINN mean solution significantly deviates from the true solution, and its uncertainty bands fail to capture the true profile. In contrast, the E-PINN method provides a more accurate mean prediction, closely following the true solution, with uncertainty bands adequately encompassing the true solution. Similarly, Dropout-PINNs yield reasonably accurate mean predictions, with uncertainty bands that widen as the dropout rate increases, consistent with the trends observed in previous cases.

In Fig. 9, corresponding to a higher sensor noise level ( $\epsilon_f \sim \mathcal{N}(0, 0.1^2)$ ), B-PINN continues to produce inaccurate mean predictions, particularly in regions with steep gradients of  $u$ . Dropout-PINNs exhibit minimal changes in uncertainty estimates despite the increased noise; however, their mean predictions deteriorate notably. Meanwhile, E-PINNs show decreased accuracy in mean predictions as sensor noise increases, along with a corresponding expansion of uncertainty bands. Table 7 summarizes the average width of the uncertainty bands for the different methods.

Tables 7 and Table 8 summarize the average width of the uncertainty bands and the empirical coverage for the different methods. The results indicate that all methods achieve empirical coverage values close to 1.00 across both noise levels for this test case, except for the B-PINN at the 10% noise level, where coverage drops significantly to 0.54. This substantial underperformance indicates that despite producing the sharpest uncertainty bounds ( $\mu_{2\sigma}^w = 0.17$ ), B-PINNs become increasingly overconfident as noise levels increase, failing to adequately capture the true uncertainty of the system. In contrast, both E-PINNs and Dropout-PINNs maintain high coverage across both noise levels, demonstrating greater robustness to increasing measurement noise in nonlinear systems, albeit at the cost of wider uncertainty bands.

Table 8: Comparison of empirical coverage  $C_\gamma$  for the 1D nonlinear Poisson equation test case

Sensor Noise	B-PINN	E-PINN	Dropout-PINN (2%)	Dropout-PINN (5%)
$\epsilon \sim \mathcal{N}(0, 0.01^2)$	<b>1.00</b>	<b>1.00</b>	<b>1.00</b>	<b>1.00</b>
$\epsilon \sim \mathcal{N}(0, 0.1^2)$	0.54	<b>1.00</b>	<b>1.00</b>	<b>1.00</b>

Table 9: Comparison of computational efficiency for uncertainty quantification methods

Test Case	B-PINN*	E-PINN*	Dropout-PINN*
Function regression	21.71	134.84	<b>135.76</b>
Poisson equation	19.40	111.54	<b>123.24</b>
Flow through porous media	18.53	117.48	<b>121.32</b>
Nonlinear Poisson equation	17.51	94.71	<b>97.95</b>

\*Values reported in iterations per second; higher values indicate better computational performance.

### 3.5 Comparison of inference times

Table 9 compares the inference speeds (in iterations per second) of the B-PINN, E-PINN, and Dropout-PINN methods across all test cases. All experiments were conducted using identical network architectures on an Nvidia RTX A2000 GPU, with B-PINN requiring 2000 Monte Carlo samples to achieve well-calibrated uncertainty estimates. The results highlight the significant computational advantage of E-PINN and Dropout-PINN over B-PINN. In fact, E-PINN and Dropout-PINN exhibit comparable computational efficiency; however, given that E-PINN delivers superior uncertainty quantification compared to Dropout-PINN for the examples tested, it presents a more favorable accuracy-efficiency trade-off.

For instance, in the function regression test, E-PINN achieved 134.84 iterations/sec, while Dropout-PINN reached 135.76 iterations/sec, significantly outperforming B-PINN, which achieved only 21.71 iterations/sec. This trend persists across all test cases. The inference time for B-PINN remains relatively constant because its computational cost is primarily determined by the fixed number of Monte Carlo samples. In contrast, the inference cost for E-PINN and Dropout-PINN depends on the complexity of the governing equations—more terms to compute result in higher per-iteration costs. Consequently, the nonlinear Poisson test case exhibits the highest inference times among all cases.

### 3.6 Ablation studies on 1D viscous Burgers’ equation

This section considers the effect of the different hyperparameters associated with the E-PINN framework on its mean and uncertainty predictions. All the ablation test cases are run on viscous Burgers’ equation tests case with a manufactured source term given by:

$$\frac{\partial u}{\partial t} + u \frac{\partial u}{\partial x} - \nu \frac{\partial^2 u}{\partial x^2} = f, \quad x \in [-1, 1] \quad \text{and} \quad t \in [0, 1], \quad (35)$$

where the viscosity  $\nu = 0.01/\pi$ . The exact solution is given by

$$u(x, t) = \sin(kx + \omega t), \quad (36)$$

where  $k = \pi$ ,  $\omega = 2$ , and  $f$  can be computed from the specified exact solution. We consider the effect of different training methodologies of the E-PINN and the underlying base PINN, data noise in the sensors for  $f$ , number of samples used to train the E-PINN epinet, as well as the number of trainable parameters.

#### 3.6.1 Effect of training method

This section examines how the training methodology impacts the uncertainty quantification generated by E-PINNs. Two training approaches are tested: the *coupled* approach, where the PINN and epinet are trained together, and the *decoupled* approach, where the epinet is trained after a pre-trained PINN. For the decoupled approach, a stop-gradient condition prevents gradients from propagating into the pre-trained PINN. In both cases, the architecture of the PINN and its companion epinet, the learning rate, the number of training epochs, and the number of sampling points are kept consistent. Sensor noise is set to  $\epsilon_f \sim \mathcal{N}(0, 0.01^2)$  for both training methodologies.

Figure 10 presents the predicted mean and uncertainty for  $u$  for the coupled and decoupled approaches at two different time instances,  $t = 0.3$  and  $t = 0.8$ . While the mean predictions for both methodologies agree well with the true solution, the coupled training approach results in a slightly narrower uncertainty band ( $\mu_{2\sigma}^w = 0.21$ ) compared to the decoupled approach ( $\mu_{2\sigma}^w = 0.26$ ). This observation suggests that training the PINN and epinet simultaneously may lead to tighter (and potentially overconfident) uncertainty estimates, possibly due to overfitting. However, despite the

Table 10: Comparison of sharpness  $\mu_{2\sigma}^w$  for the different training methods

Training method	Coupled	Decoupled
$\mu_{2\sigma}^w$	<b>0.21</b>	0.26

Table 11: Comparison of sharpness  $\mu_{2\sigma}^w$  for different sensor noise levels

Sensor Noise	$\epsilon_f, \epsilon_u \sim \mathcal{N}(0, 0.01^2)$	$\epsilon_f, \epsilon_u \sim \mathcal{N}(0, 0.1^2)$	$\epsilon_f, \epsilon_u \sim \mathcal{N}(0, 0.3^2)$
$\mu_{2\sigma}^w$	0.26	0.53	1.05

marginally smaller sharpness at a similar coverage (c.f. Fig. 10), coupled training has the disadvantage of increased computational time since the PINN must be re-trained, whereas in the decoupled case only the epinet is trained. This makes the decoupled approach more attractive in scenarios where computational efficiency is a priority.

### 3.6.2 Effect of sensor noise

This section studies the effect of the noise added to the sensor measurements for  $f$  in the interior of the domain ( $\epsilon_f$ ) and  $u$  at the boundaries ( $\epsilon_u$ ). Both  $\epsilon_f$  and  $\epsilon_u$  are drawn from zero-mean normal distributions with different variances. All tests are conducted using the decoupled training approach, while both the number of sampling points and the network architecture are kept fixed.

Figure 11 illustrates the predicted mean and uncertainty for  $u$  at two distinct time instances,  $t = 0.3$  s and  $t = 0.8$  s. The figure clearly demonstrates that as the sensor noise ( $\epsilon_f$  and  $\epsilon_u$ ) increases, the uncertainty bands grow correspondingly, which aligns with expected behavior.

### 3.6.3 Effect of number of collocation points

This section studies the effect of the number of collocation points ( $n_f$ ) used for training the base PINN network and the epinet. The training approach and network sizes were kept constant and sensor noise is set to  $\epsilon_f \sim \mathcal{N}(0, 0.01^2)$  for all cases.

Figure 12 illustrates the effect of varying the number of collocation points on the uncertainty predictions. As the number of collocation points increases from  $n_f = 20$  to  $n_f = 100$ , the width of the uncertainty bands decreases. However, beyond  $n_f = 100$ , further increasing the number of collocation points to  $n_f = 500$  does not result in any significant change in the uncertainty bands. This suggests that there is a minimum threshold of collocation points required to effectively calibrate the epinet, beyond which additional points do not significantly impact uncertainty predictions. We note, however, that this minimum threshold is likely problem-dependent.

### 3.6.4 Effect of number of E-PINN network parameters

This section examines the impact of the number of network parameters in the epinet by varying the number of hidden units,  $H$ , in each layer. The training methodology and the number of training iterations were kept constant, and no noise was introduced into the sensor measurements for  $f$  and  $u$ . While the number of layers in the epinet was fixed at two, the number of hidden units per layer was systematically varied to study the effect.

Figure 13 demonstrates that increasing the number of hidden units from  $H = 4$  to  $H = 16$  results in a noticeable reduction in the uncertainty bands. However, further increasing  $H$  to  $H = 32$  and  $H = 64$  does not lead to any significant changes in the predicted uncertainty. This indicates that a minimum level of expressivity, determined by the number of parameters in the epinet, is required to accurately capture uncertainty. Beyond this threshold, further increasing the number of parameters has negligible impact on uncertainty predictions.

Table 12: Comparison of sharpness  $\mu_{2\sigma}^w$  for different number of collocation points

Collocation Points	$n_f = 20$	$n_f = 100$	$n_f = 500$
$\mu_{2\sigma}^w$	0.33	<b>0.26</b>	0.28

Table 13: Comparison of sharpness  $\mu_{2\sigma}^w$  for different number of E-PINN network parameters

Network Parameters	$H = 4$	$H = 16$	$H = 32$	$H = 64$
$\mu_{2\sigma}^w$	0.42	<b>0.26</b>	0.29	0.27

## 4 Conclusions

This work introduces E-PINNs, a novel framework that extends traditional PINNs by efficiently quantifying total uncertainty. By incorporating a smaller, supplementary neural network called the epinet, E-PINNs provide a computationally efficient alternative to existing uncertainty quantification methods. While B-PINNs offer a comprehensive framework for capturing both uncertainties through Bayesian inference, they require substantial computational resources for posterior sampling. Similarly, while Dropout-PINNs provide a simpler approach to uncertainty quantification, their effectiveness is highly dependent on hyperparameter selection.

A key theoretical distinction between B-PINNs and E-PINNs lies in their treatment of uncertainty sources. While B-PINNs capture both uncertainties through a unified Bayesian treatment that combines data noise and parameter uncertainty in the posterior distribution, E-PINNs achieve this through a hierarchical structure: epistemic uncertainty arises from variations across different epistemic indices, while aleatoric uncertainty is captured by the inherent variability within each index due to noisy measurements or source terms. This architecture enables E-PINNs to naturally decompose the total predictive uncertainty into its epistemic and aleatoric components while maintaining computational efficiency.

Extensive evaluations of E-PINNs were conducted across multiple test cases involving forward problems with PDEs. These results demonstrate that E-PINNs produce uncertainty estimates that are both accurate and computationally efficient. Comparative analyses show that while B-PINNs provide comprehensive uncertainty quantification at higher computational costs, and Dropout-PINNs are sensitive to hyperparameters like dropout rate, E-PINNs provide well-calibrated uncertainty estimates while maintaining computational scalability.

Ablation studies further explored the sensitivity of E-PINNs to key hyperparameters, such as the number of collocation points, network parameters, and training strategies. It was observed that a minimum threshold of collocation points is required to calibrate the epinet effectively, beyond which additional points do not significantly affect uncertainty predictions. Similarly, while increasing the number of parameters in the epinet enhances its expressivity and reduces sharpness, further increases beyond a certain point yield diminishing returns in terms of uncertainty. The study also compared coupled and decoupled training approaches, finding that the decoupled method, where the epinet is trained on a pre-trained PINN, produced only marginally wider (and thus more conservative) uncertainty bands while maintaining similar coverage and significantly lower computational costs. These findings highlight the flexibility and adaptability of E-PINNs in capturing uncertainty efficiently without unnecessary computational overhead.

In summary, E-PINNs represent a significant advancement in uncertainty quantification for PINNs, offering a computationally efficient approach to estimate total uncertainty. The framework achieves this through a hierarchical structure that provides comprehensive uncertainty treatment while avoiding high computational costs associated with posterior sampling and re-training. This approach has the potential to broaden the applicability of PINNs in scientific and engineering domains where reliable predictions and confidence estimates are essential. Future research will aim to extend E-PINNs to more complex and high-dimensional systems, as well as to validate their performance in real-world applications where uncertainty quantification is critical for decision-making and risk assessment.

## 5 Code and data availability

All code, trained models, and data required to replicate the examples presented in this paper will be released upon publication.

## 6 Acknowledgements

This project was completed with support from the U.S. Department of Energy, Advanced Scientific Computing Research program, under the "Resolution-invariant deep learning for accelerated propagation of epistemic and aleatory uncertainty in multi-scale energy storage systems, and beyond" project (Project No. 81824) and under the "Uncertainty Quantification for Multifidelity Operator Learning (MOLUcQ)" project (Project No. 81739). The computational work was performed using PNNL Institutional Computing at Pacific Northwest National Laboratory. Pacific Northwest



National Laboratory (PNNL) is a multi-program national laboratory operated for the U.S. Department of Energy (DOE) by Battelle Memorial Institute under Contract No. DE-AC05-76RL01830.

## References

- [1] M. Raissi, P. Perdikaris, G. E. Karniadakis, Physics-informed neural networks: A deep learning framework for solving forward and inverse problems involving nonlinear partial differential equations, *Journal of Computational physics* 378 (2019) 686–707.
- [2] X. Jin, S. Cai, H. Li, G. E. Karniadakis, Nsfnets (navier-stokes flow nets): Physics-informed neural networks for the incompressible navier-stokes equations, *Journal of Computational Physics* 426 (2021) 109951.
- [3] S. Cai, Z. Mao, Z. Wang, M. Yin, G. E. Karniadakis, Physics-informed neural networks (pinns) for fluid mechanics: A review, *Acta Mechanica Sinica* 37 (12) (2021) 1727–1738.
- [4] S. Hanrahan, M. Kozul, R. D. Sandberg, Studying turbulent flows with physics-informed neural networks and sparse data, *International Journal of Heat and Fluid Flow* 104 (2023) 109232.
- [5] Y. Patel, V. Mons, O. Marquet, G. Rigas, Turbulence model augmented physics-informed neural networks for mean-flow reconstruction, *Physical Review Fluids* 9 (3) (2024) 034605.
- [6] R. Laubscher, Simulation of multi-species flow and heat transfer using physics-informed neural networks, *Physics of Fluids* 33 (8).
- [7] J. Xu, H. Wei, H. Bao, Physics-informed neural networks for studying heat transfer in porous media, *International Journal of Heat and Mass Transfer* 217 (2023) 124671.
- [8] S. Cai, Z. Wang, S. Wang, P. Perdikaris, G. E. Karniadakis, Physics-informed neural networks for heat transfer problems, *Journal of Heat Transfer* 143 (6) (2021) 060801.
- [9] D. Jalili, S. Jang, M. Jadidi, G. Giustini, A. Keshmiri, Y. Mahmoudi, Physics-informed neural networks for heat transfer prediction in two-phase flows, *International Journal of Heat and Mass Transfer* 221 (2024) 125089.
- [10] F. Sahli Costabal, Y. Yang, P. Perdikaris, D. E. Hurtado, E. Kuhl, Physics-informed neural networks for cardiac activation mapping, *Frontiers in Physics* 8 (2020) 42.
- [11] G. Kissas, Y. Yang, E. Hwuang, W. R. Witschey, J. A. Detre, P. Perdikaris, Machine learning in cardiovascular flows modeling: Predicting arterial blood pressure from non-invasive 4d flow mri data using physics-informed neural networks, *Computer Methods in Applied Mechanics and Engineering* 358 (2020) 112623.
- [12] K. Sel, A. Mohammadi, R. I. Pettigrew, R. Jafari, Physics-informed neural networks for modeling physiological time series for cuffless blood pressure estimation, *npj Digital Medicine* 6 (1) (2023) 110.
- [13] A. Khan, D. A. Lowther, Physics informed neural networks for electromagnetic analysis, *IEEE Transactions on Magnetism* 58 (9) (2022) 1–4.
- [14] M. Baldan, P. Di Barba, D. A. Lowther, Physics-informed neural networks for inverse electromagnetic problems, *IEEE Transactions on Magnetism* 59 (5) (2023) 1–5.
- [15] L. Yang, X. Meng, G. E. Karniadakis, B-pinns: Bayesian physics-informed neural networks for forward and inverse pde problems with noisy data, *Journal of Computational Physics* 425 (2021) 109913.
- [16] A. Der Kiureghian, O. Ditlevsen, Aleatory or epistemic? does it matter?, *Structural safety* 31 (2) (2009) 105–112.
- [17] E. Hüllermeier, W. Waegeman, Aleatoric and epistemic uncertainty in machine learning: An introduction to concepts and methods, *Machine learning* 110 (3) (2021) 457–506.
- [18] D. J. MacKay, A practical bayesian framework for backpropagation networks, *Neural computation* 4 (3) (1992) 448–472.
- [19] A. Graves, Practical variational inference for neural networks, *Advances in neural information processing systems* 24.
- [20] R. M. Neal, *Bayesian learning for neural networks*, Vol. 118, Springer Science & Business Media, 2012.
- [21] C. Blundell, J. Cornebise, K. Kavukcuoglu, D. Wierstra, Weight uncertainty in neural network, in: International conference on machine learning, PMLR, 2015, pp. 1613–1622.
- [22] B. Lakshminarayanan, A. Pritzel, C. Blundell, Simple and scalable predictive uncertainty estimation using deep ensembles, *Advances in neural information processing systems* 30.
- [23] S. Fort, H. Hu, B. Lakshminarayanan, Deep ensembles: A loss landscape perspective, *arXiv preprint arXiv:1912.02757*.

- [24] A. Ashukha, A. Lyzhov, D. Molchanov, D. Vetrov, Pitfalls of in-domain uncertainty estimation and ensembling in deep learning, *arXiv preprint arXiv:2002.06470*.
- [25] G. E. Hinton, N. Srivastava, A. Krizhevsky, I. Sutskever, R. R. Salakhutdinov, Improving neural networks by preventing co-adaptation of feature detectors, *arXiv preprint arXiv:1207.0580*.
- [26] Y. Gal, Z. Ghahramani, Dropout as a bayesian approximation: Representing model uncertainty in deep learning, in: international conference on machine learning, PMLR, 2016, pp. 1050–1059.
- [27] Y. Gal, J. Hron, A. Kendall, Concrete dropout, *Advances in neural information processing systems* 30.
- [28] Y. Li, Y. Gal, Dropout inference in bayesian neural networks with alpha-divergences, in: International conference on machine learning, PMLR, 2017, pp. 2052–2061.
- [29] T. Hiraoka, T. Imagawa, T. Hashimoto, T. Onishi, Y. Tsuruoka, Dropout q-functions for doubly efficient reinforcement learning, *arXiv preprint arXiv:2110.02034*.
- [30] L. Yang, D. Zhang, G. E. Karniadakis, Physics-informed generative adversarial networks for stochastic differential equations, *SIAM Journal on Scientific Computing* 42 (1) (2020) A292–A317.
- [31] Z. Zou, X. Meng, A. F. Psaros, G. E. Karniadakis, Neuraluq: A comprehensive library for uncertainty quantification in neural differential equations and operators, *SIAM Review* 66 (1) (2024) 161–190.
- [32] D. Zhang, L. Lu, L. Guo, G. E. Karniadakis, Quantifying total uncertainty in physics-informed neural networks for solving forward and inverse stochastic problems, *Journal of Computational Physics* 397 (2019) 108850.
- [33] L. Lu, P. Jin, G. E. Karniadakis, DeepoNet: Learning nonlinear operators for identifying differential equations based on the universal approximation theorem of operators, *arXiv preprint arXiv:1910.03193*.
- [34] Y. Yang, G. Kissas, P. Perdikaris, Scalable uncertainty quantification for deep operator networks using randomized priors, *Computer Methods in Applied Mechanics and Engineering* 399 (2022) 115399.
- [35] A. Pensoneault, X. Zhu, Uncertainty quantification for deepoNets with ensemble kalman inversion, *Journal of computational physics* 523 (2025) 113670.
- [36] S. Garg, S. Chakraborty, Vb-deepoNet: A bayesian operator learning framework for uncertainty quantification, *Engineering Applications of Artificial Intelligence* 118 (2023) 105685.
- [37] Z. Zhang, C. Moya, W. T. Leung, G. Lin, H. Schaeffer, Bayesian deep operator learning for homogenized to fine-scale maps for multiscale pde, *Multiscale Modeling & Simulation* 22 (3) (2024) 956–972.
- [38] L. Podina, M. T. Rad, M. Kohandel, Conformalized physics-informed neural networks, *arXiv preprint arXiv:2405.08111*.
- [39] C. Moya, A. Mollaali, Z. Zhang, L. Lu, G. Lin, Conformalized-deepoNet: A distribution-free framework for uncertainty quantification in deep operator networks, *Physica D: Nonlinear Phenomena* 471 (2025) 134418.
- [40] A. Angelopoulos, S. Bates, J. Malik, M. I. Jordan, Uncertainty sets for image classifiers using conformal prediction, *arXiv preprint arXiv:2009.14193*.
- [41] I. Osband, Z. Wen, S. M. Asghari, V. Dwaracherla, M. Ibrahimi, X. Lu, B. Van Roy, Epistemic neural networks, *Advances in Neural Information Processing Systems* 36 (2023) 2795–2823.
- [42] X. Meng, H. Babaei, G. E. Karniadakis, Multi-fidelity bayesian neural networks: Algorithms and applications, *Journal of Computational Physics* 438 (2021) 110361.
- [43] G. Lin, Y. Wang, Z. Zhang, Multi-variance replica exchange sgMCMC for inverse and forward problems via bayesian PINN, *Journal of Computational Physics* 460 (2022) 111173.
- [44] A. Pensoneault, X. Zhu, Efficient bayesian physics informed neural networks for inverse problems via ensemble kalman inversion, *Journal of Computational Physics* 508 (2024) 113006.
- [45] R. M. Neal, MCMC using hamiltonian dynamics, *arXiv preprint arXiv:1206.1901*.
- [46] N. Srivastava, G. Hinton, A. Krizhevsky, I. Sutskever, R. Salakhutdinov, Dropout: a simple way to prevent neural networks from overfitting, *The journal of machine learning research* 15 (1) (2014) 1929–1958.
- [47] J. Yao, W. Pan, S. Ghosh, F. Doshi-Velez, Quality of uncertainty quantification for bayesian neural network inference, *arXiv preprint arXiv:1906.09686*.
- [48] K. He, X. Zhang, S. Ren, J. Sun, Delving deep into rectifiers: Surpassing human-level performance on imagenet classification, in: Proceedings of the IEEE international conference on computer vision, 2015, pp. 1026–1034.
- [49] L. D. McClenny, U. M. Braga-Neto, Self-adaptive physics-informed neural networks, *Journal of Computational Physics* 474 (2023) 111722.

- [50] S. J. Anagnostopoulos, J. D. Toscano, N. Stergiopoulos, G. E. Karniadakis, Residual-based attention in physics-informed neural networks, *Computer Methods in Applied Mechanics and Engineering* 421 (2024) 116805.
- [51] W. Chen, A. A. Howard, P. Stinis, Self-adaptive weights based on balanced residual decay rate for physics-informed neural networks and deep operator networks, *arXiv preprint arXiv:2407.01613*.
- [52] T. Gneiting, F. Balabdaoui, A. E. Raftery, Probabilistic forecasts, calibration and sharpness, *Journal of the Royal Statistical Society Series B: Statistical Methodology* 69 (2) (2007) 243–268.
- [53] T. Pearce, A. Brintrup, M. Zaki, A. Neely, High-quality prediction intervals for deep learning: A distribution-free, ensembled approach, in: International conference on machine learning, PMLR, 2018, pp. 4075–4084.
- [54] A. Khosravi, S. Nahavandi, D. Creighton, A. F. Atiya, Comprehensive review of neural network-based prediction intervals and new advances, *IEEE Transactions on neural networks* 22 (9) (2011) 1341–1356.

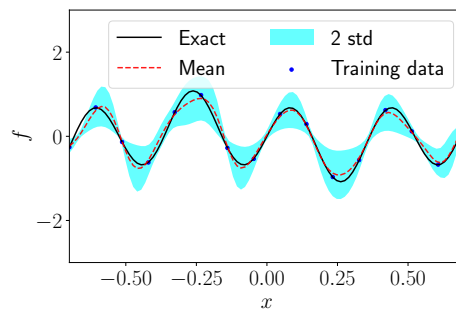
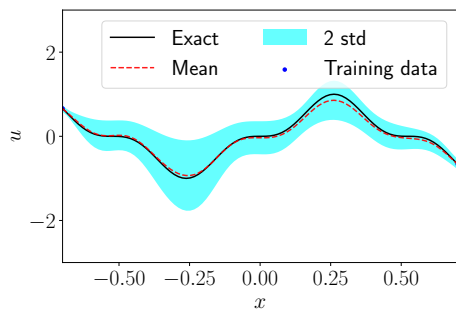
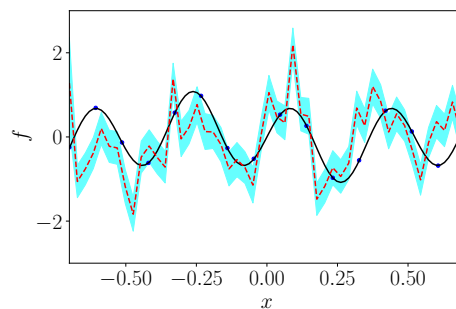
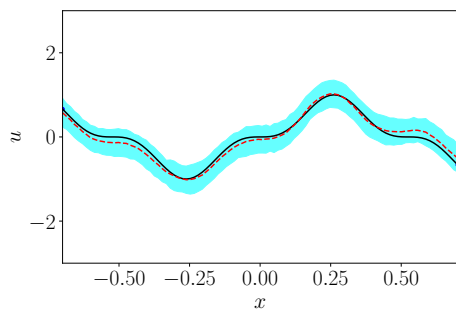
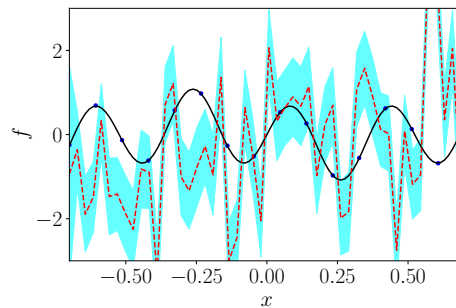
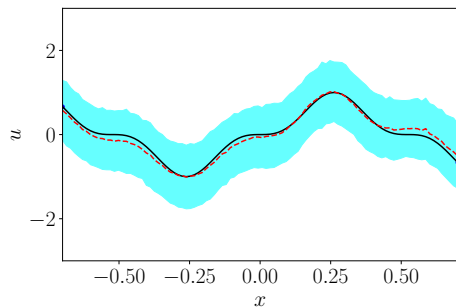
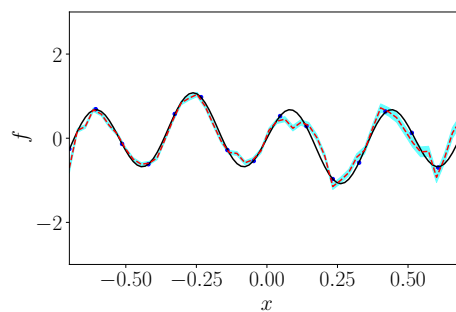
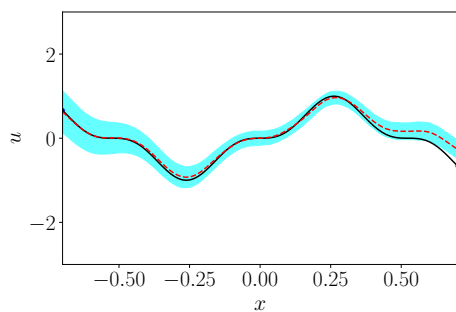
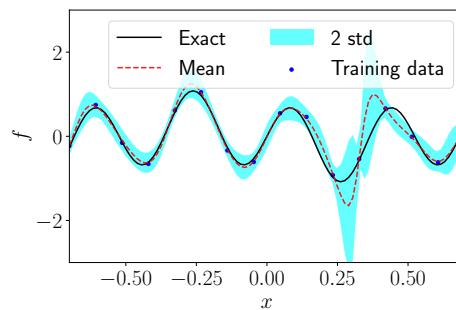
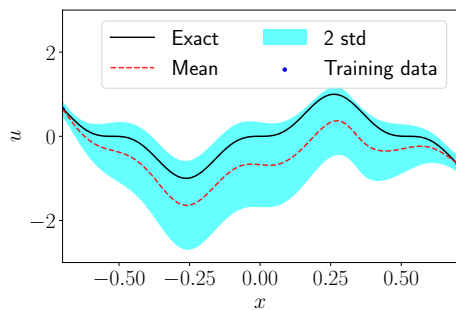
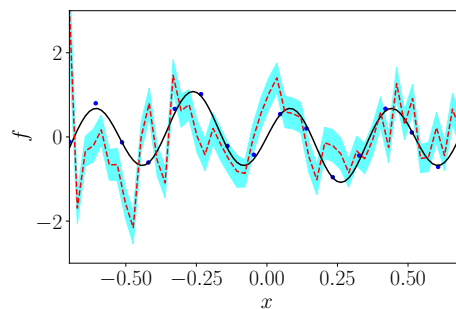
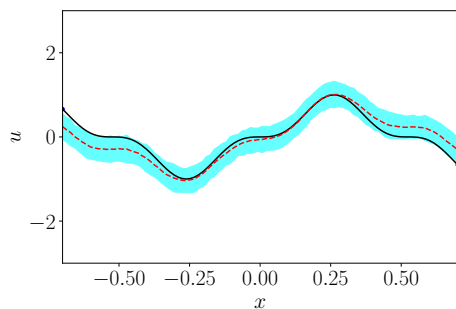
(a) B-PINN,  $u$  (left),  $f$  (right).(b) Dropout-PINN with 2% drop rate,  $u$  (left),  $f$  (right).(c) Dropout-PINN with 5% drop rate,  $u$  (left),  $f$  (right).(d) E-PINN,  $u$  (left),  $f$  (right).

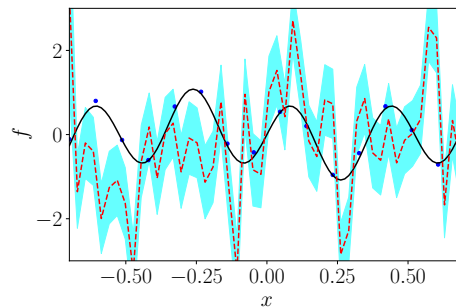
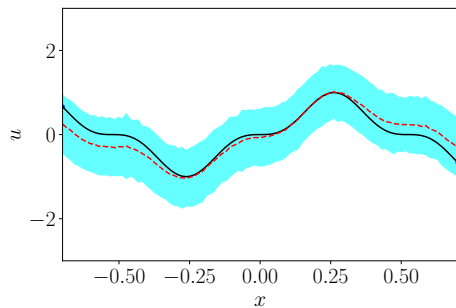
Figure 4: Mean and uncertainty predictions for  $u$  and  $f$  in a 1D Poisson equation test case with  $\epsilon_f \sim \mathcal{N}(0, 0.01^2)$  using (a) B-PINN (b) Dropout-PINN with 2% drop rate (c) Dropout-PINN with 5% drop rate (d) E-PINN.



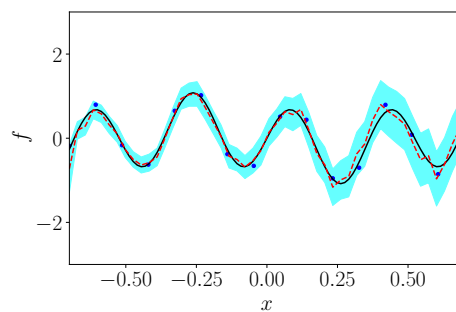
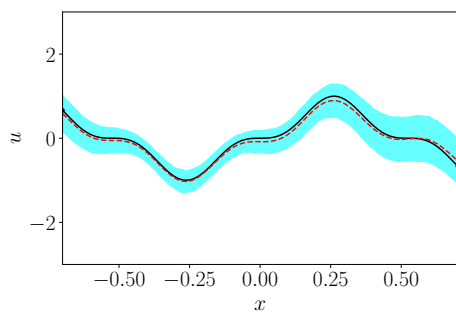
(a) B-PINN,  $u$  (left),  $f$  (right).



(b) Dropout-PINN with 2% drop rate,  $u$  (left),  $f$  (right).



(c) Dropout-PINN with 5% drop rate,  $u$  (left),  $f$  (right).



(d) E-PINN,  $u$  (left),  $f$  (right).

Figure 5: Mean and uncertainty predictions for  $u$  and  $f$  in a 1D Poisson equation test case with  $\epsilon_f \sim \mathcal{N}(0, 0.1^2)$  using (a) B-PINN (b) Dropout-PINN with 2% drop rate (c) Dropout-PINN with 5% drop rate (d) E-PINN.

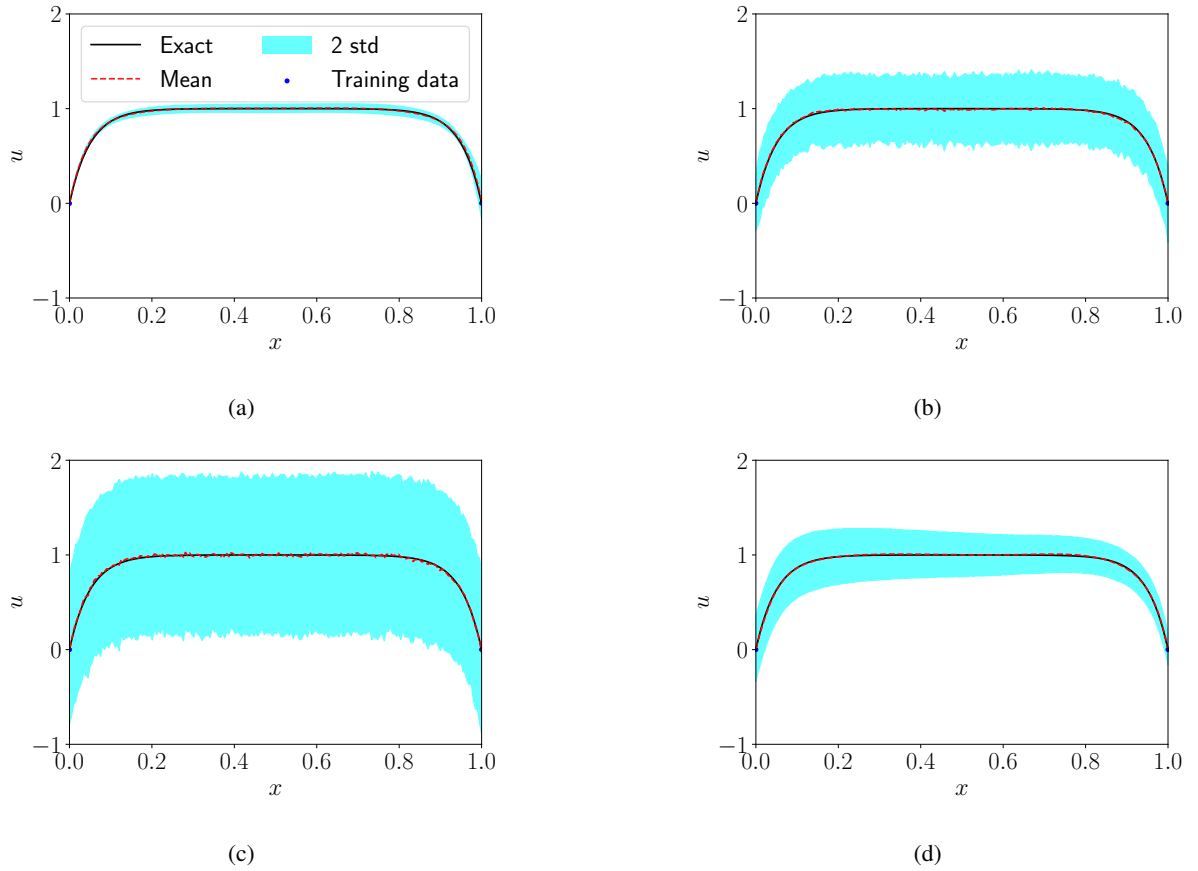


Figure 6: Mean and uncertainty predictions for  $u$  in a 1D flow through a porous media test case with  $\epsilon_f \sim \mathcal{N}(0, 0.01^2)$  using (a) B-PINN (b) Dropout-PINNs with 2% drop rate (c) Dropout-PINNs with 5% drop rate (d) E-PINNs.

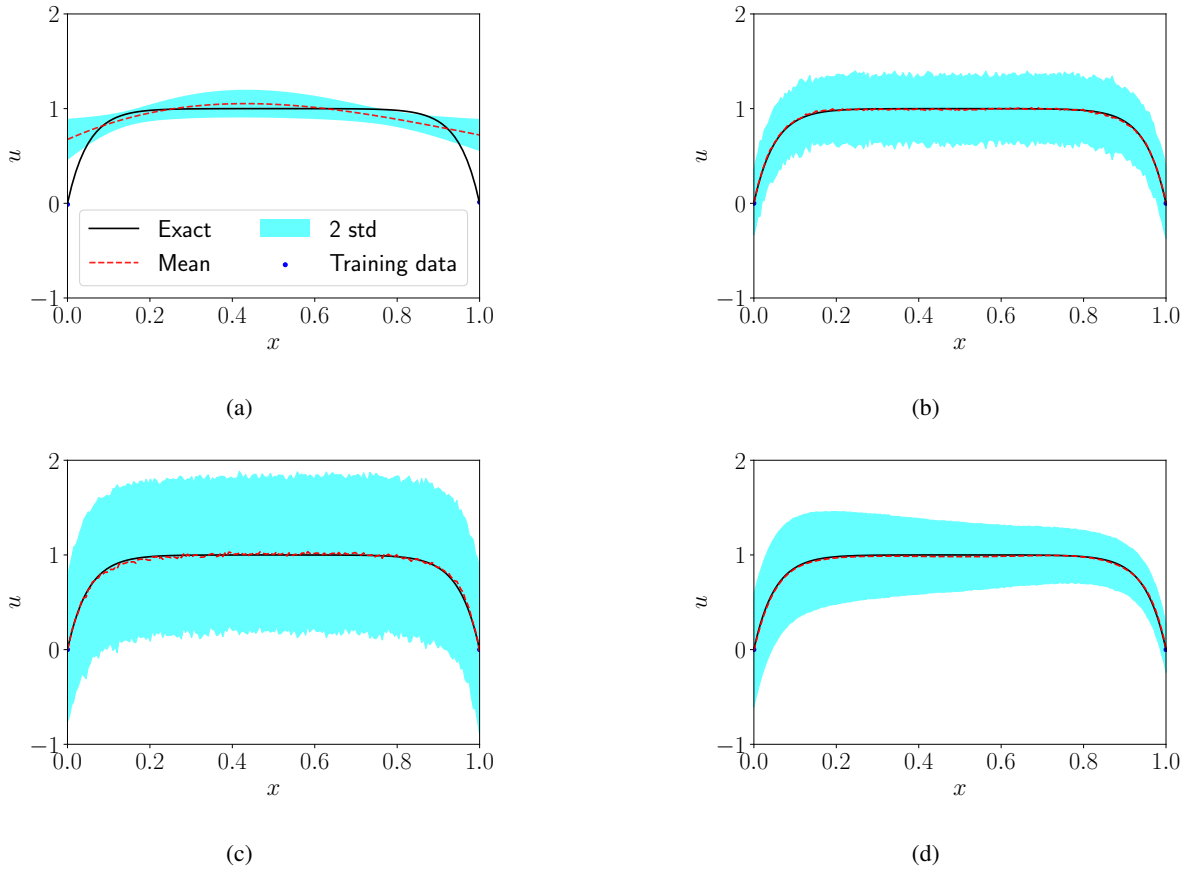


Figure 7: Mean and uncertainty predictions for  $u$  in a 1D flow through a porous media test case with  $\epsilon_f \sim \mathcal{N}(0, 0.1^2)$  using (a) B-PINN (b) Dropout-PINNs with 2% drop rate (c) Dropout-PINNs with 5% drop rate (d) E-PINN.

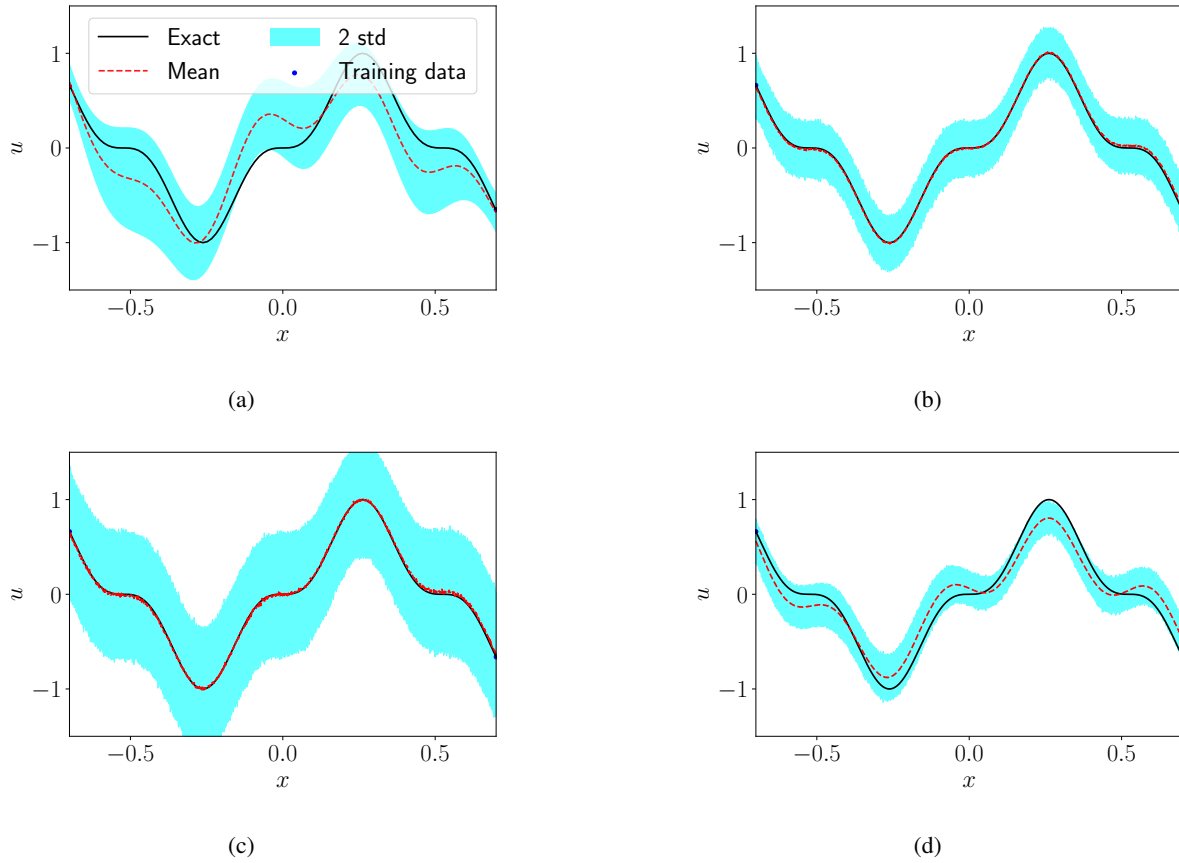


Figure 8: Mean and uncertainty predictions for  $u$  in a 1D nonlinear Poisson equation test case with  $\epsilon \sim \mathcal{N}(0, 0.01^2)$  using (a) B-PINN (b) Dropout-PINN with 2% drop rate (c) Dropout-PINN with 5% drop rate (d) E-PINN.



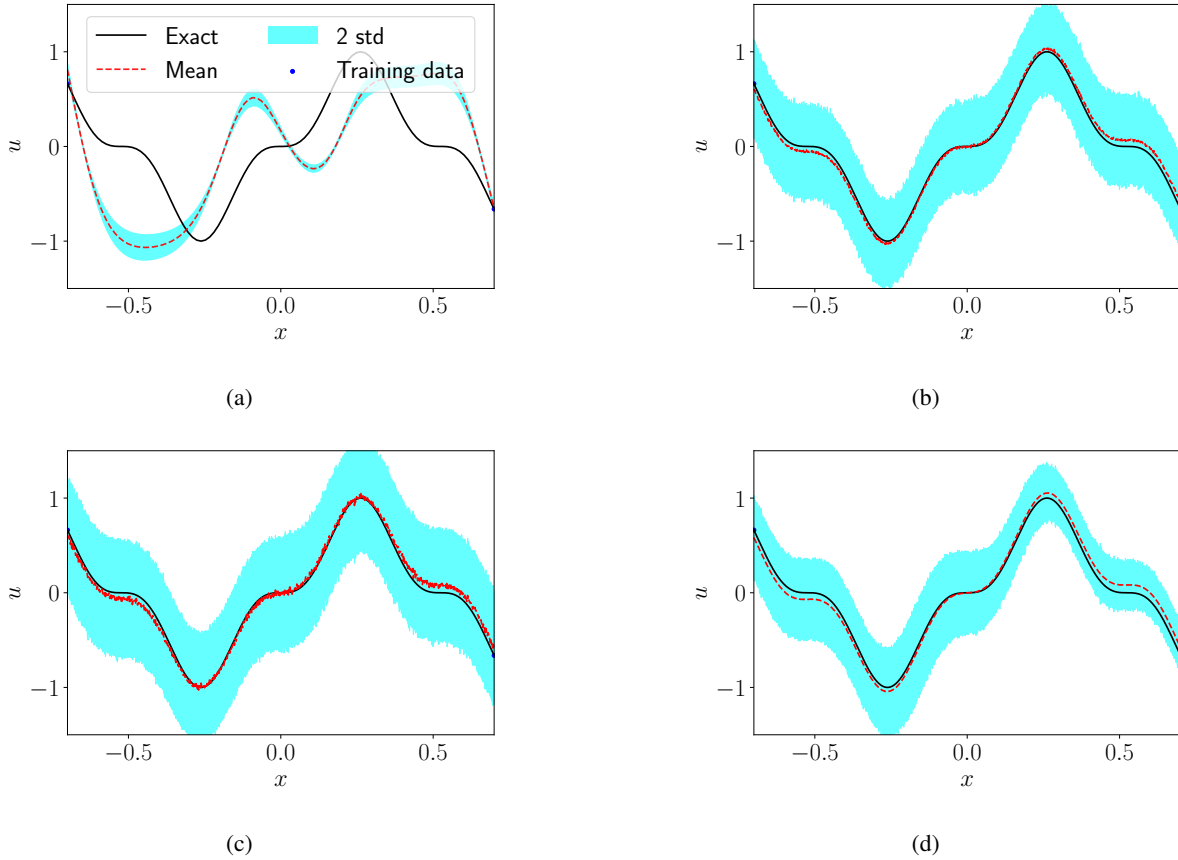


Figure 9: Mean and uncertainty predictions for  $u$  in a 1D nonlinear Poisson equation test case with  $\epsilon_f \sim \mathcal{N}(0, 0.1^2)$  using (a) B-PINN (b) Dropout-PINN with 2% drop rate (c) Dropout-PINN with 5% drop rate (d) E-PINN.

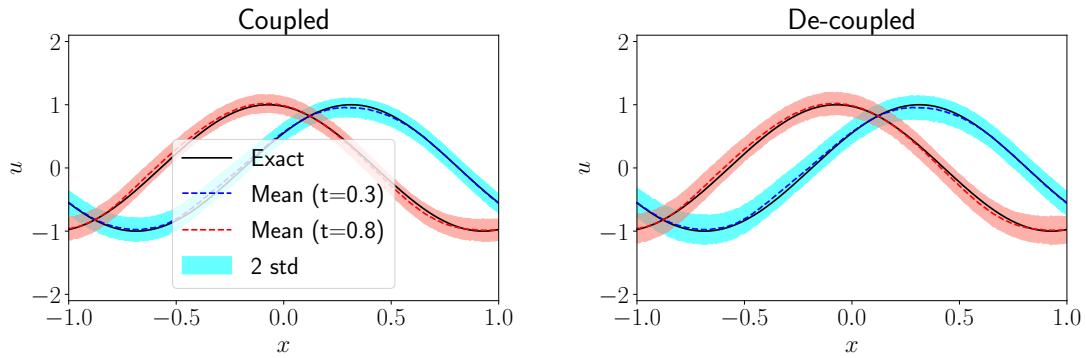


Figure 10: Comparison of the predicted mean and uncertainties in  $u$  for coupled and decoupled training approaches.

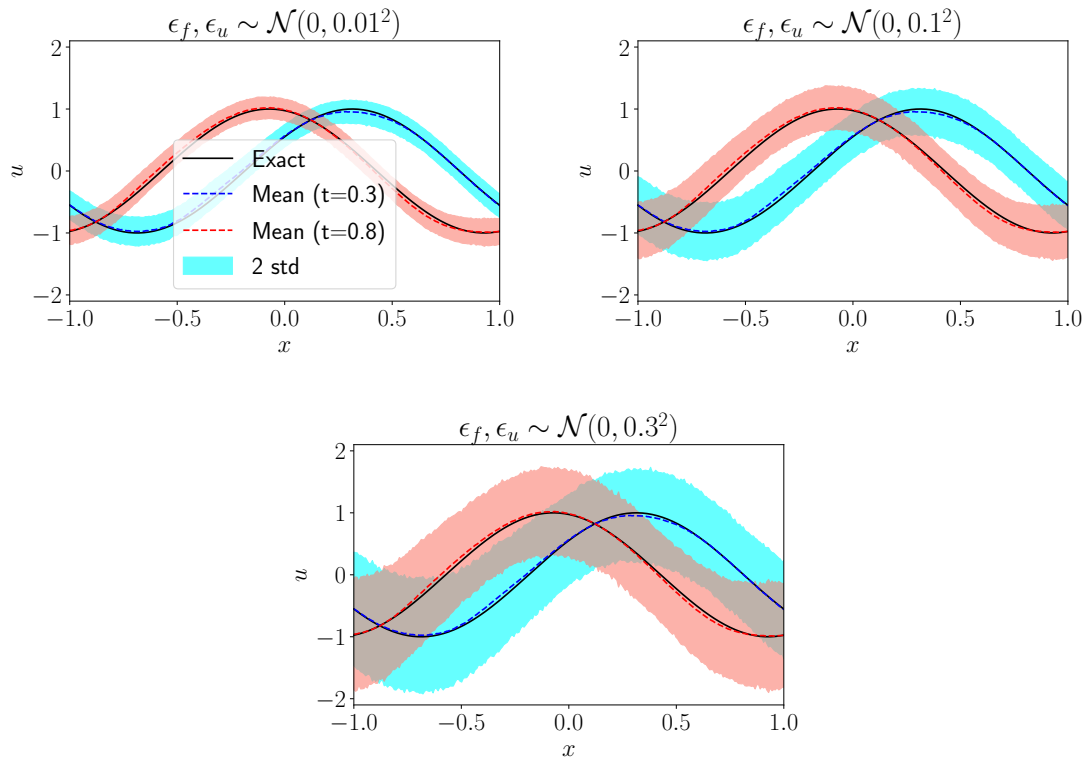


Figure 11: Comparison of the predicted mean and uncertainties in  $u$  for different sensor measurement noise ( $\epsilon_f, \epsilon_u$ ) levels.

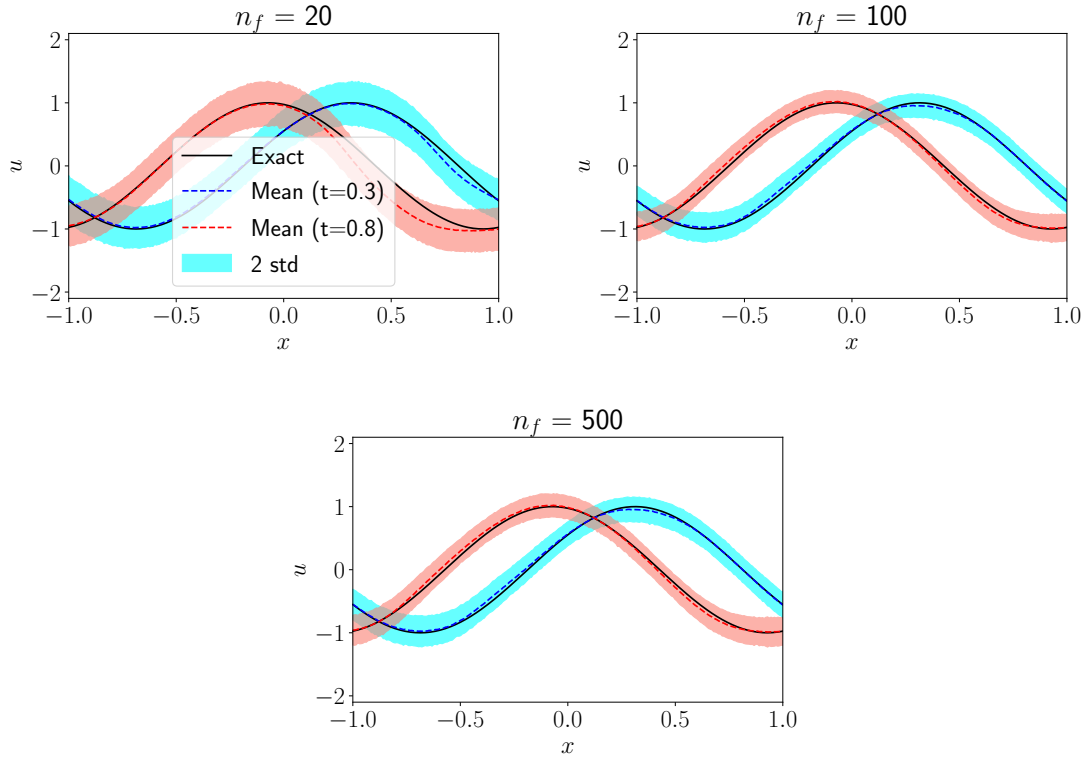


Figure 12: Effect of number of training points

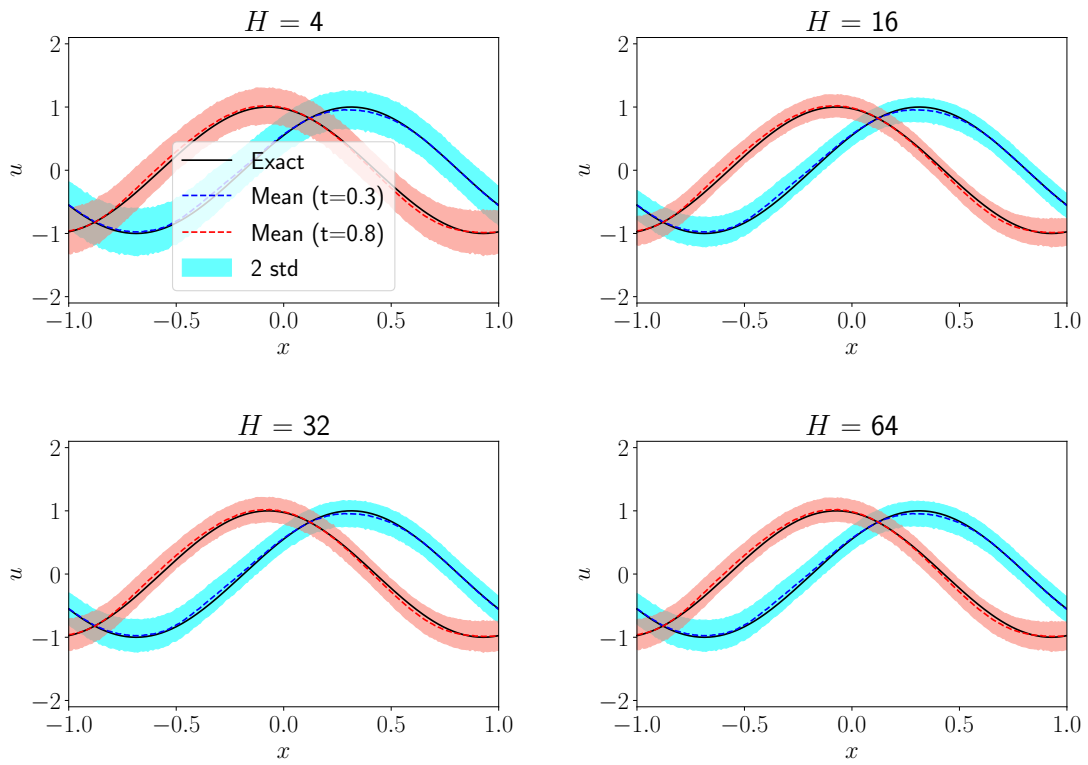


Figure 13: Effect of number of parameters in the epinet.